Applied Catalysis A-GENERAL ***468:*** *pp 250-259 (2013)* ***(ISSN 0926-860X)***

Sol-derived AuNi/MgAl2O4 catalysts: formation, structure and activity in dry reforming of methane

A. Horváth[1]* L. Guczi[1]♣, A. Kocsonya[1], G. Sáfrán[2], V. La Parola[3], L. F. Liotta[3], G. Pantaleo[3], A. M. Venezia[3]*

[1]Dept. of Surface Chemistry and Catalysis, Centre for Energy Research, HAS, P.O. Box 49, H-1525 Budapest, Hungary; [2]Institute for Technical Physics and Materials Science, Research Centre for Natural Sciences, HAS, P.O. Box 49, H-1525 Budapest, Hungary, [3]ISMN- CNR, Via Ugo la Malfa 153, Palermo, I-90146

Abstract

Ni nanoparticles doped with different amount of gold were supported on $MgAl_2O_4$ by deposition from aqueous metal sol producing a series of catalysts with different Au content. The sol procedure allowed to obtain dispersed metal particles with different composition. The particle size and the particle composition of the sol was maintained even after being deposited on the support. The catalysts, characterized by several techniques such as TPR, XPS, XRD, TEM, HRTEM and EELS at the different stages of their life exhibited significant structural modification. In particular, thermal treatments in reducing and oxidizing environment produced NiAu alloy phases and NiO surface segregation, respectively. When testing for methane dry reforming with CO_2 in temperature ramped reaction, the monometallic nickel catalyst was more active at lower temperature whereas the bimetallic catalysts were more active at higher temperature. The presence of gold slightly affected the CO/H_2 ratio due to the occurrence of parallel reactions such as the reverse water gas shift reaction (RWGS). Both types of catalysts, monometallic and bimetallic ones, deactivated a little with time but the degree of activity loss was not in straightforward relation with Au content due to the different effect of gold on the stability and on the amount of carbon formation.

Keywords: Dry reforming, Methane, Nickel catalysts, $MgAl_2O_4$ support, Gold effect.

* Corresponding authors: e-mail: horvath.anita@energia.mta.hu; venezia@pa.ismn.cnr.it;
♣ Prof. L. Guczi passed away on December 20th 2012.

1. Introduction

Reforming of methane with CO_2, known also as dry reforming (DRM), is a convenient and feasible process to produce synthesis gas and at the same time to remove two powerful greenhouse gases like CO_2 and CH_4, from the environment [1-3]. As compared to the steam reforming of methane, producing syngas with a H_2/CO ratio of 3, the DRM produces a synthesis gas with the H_2/CO molar ratio close to unity, making it useful feed for the Fisher Tropsch syntheses to liquid hydrocarbons and for the syntheses of oxygenates [4]. The DRM reaction (1) is endothermic and requires high temperatures to attain good conversion levels

$CH_4 + CO_2 \rightarrow 2CO + 2\,H_2\ \Delta H°_{700°C} = 258$ kJ/mol (1)

at high temperatures the following endothermic reactions (2) and (3) referred as decomposition of methane and reverse water gas shift (RWGS), respectively, are also favored.

$CH_4 \rightarrow C + 2H_2\ \Delta H°_{700°C} = 85$ kJ/mol (2)

$CO_2 + H_2 \rightarrow CO + H_2O\ \Delta H°_{700°C} = 38$ kJ/mol (3)

For the dry reforming of methane noble metals have been successfully used providing stable and active catalysts at the lowest as possible temperatures [5]. However, because of their high cost and low availability, most of the applications are based on the use of the group VIII

transition metals [6]. Among these, Ni has been studied extensively, being the most active, cheap and available metal [7-9]. However, its main drawback is represented by the production of significant amount of carbon and by the sintering at the high temperatures of the reaction. Carbon deposits are formed when the rate of methane dissociation is faster than the oxidation of carbon, occurring with the surface oxygen species arising from CO_2 dissociation on the metal component or from carbonates formed at the metal support interface. Both, the amount and the type of carbon deposited from methane decomposition during the dry reforming, would affect the activity/stability of the Ni based catalysts [9-10]. Researchers, through the use of several surface techniques have shown different types of carbon deposits such as, polymeric, filamentous, graphitic carbon and bulk nickel carbide [10-14]. The strategies adopted to decrease the carbon poisoning include the support formulation, the support morphology and the doping of the nickel catalysts with other elements such as alkali metals, sulfur and also gold. The dry reforming of methane over nickel catalysts is generally considered structure sensitive, therefore Ni dispersion should be maintained as high as possible through the use of proper supports [15]. The $MgAl_2O_4$ spinel oxide is highly stable and thermally resistant, furthermore, it can ensure strong metal-support interaction favoring the higher metal dispersion. Additionally, in virtue of its basic nature this support will enhance the chemisorption of the CO_2 which is beneficial for the catalytic activity providing the oxygen to form CO and also favoring the elimination of the coke [16].

The addition of a noble metal such as Pt and Rh has been reported to increase the resistance of the nickel catalysts to the deactivation by carbon [5,11,17-19]. The effect of the addition of gold has been mainly studied in the steam reforming of hydrocarbons [14,20-21]. In such reaction the decrease of reactivity upon dilution of Ni sites with the less reactive Au metal, was counterbalanced by the positive effect of a lower deactivation by carbon in the presence of gold. This effect was attributed to the formation of a surface NiAu alloy with the Au preferentially located at the high- energy steps and edges sites where the carbon nucleation over nickel is supposed to initiate [14]. In contrast, in the case of the dry reforming of methane, the modification of the nickel catalysts by gold has received less attention and furthermore, with controversial results. The positive role of gold for a series of $Ni/MgAl_2O_4$ catalysts prepared by wet impregnation was described [13]. On the contrary a recent study on alumina supported nickel and gold – doped nickel catalyst did not provide any experimental evidence for the beneficial effect of gold [10]. Probably the influence of the gold and generally of a second metal, is mediated by other factors such as the catalyst preparation method, the relative amount of the active site components and the support formulation.

In order to verify the role of gold in nickel catalysts used for the CO_2 reforming of methane, bimetallic Ni-Au catalysts supported over commercial $MgAl_2O_4$ spinel were prepared by a non conventional sol method. Intending to selectively inhibit the carbon formation without affecting much the activity, different atomic Au/Ni ratios were considered. The choice of the sol procedure aimed to the formation of highly dispersed metal particles with well defined structure and the close proximity of generally immiscible Ni and Au phases.

2. Experimental

2.1. Sample preparation

Aqueous solutions of $HAuCl_4 \cdot 3H_2O$(Aldrich), 20 wt% poly(diallyldimethylammonium) chloride (PDDA) in water (Aldrich), nickel(II) nitrate hexahydrate (Aldrich), tannic acid (Aldrich), sodium-citrate (Aldrich), freshly dissolved sodium borohydride, and commercial $MgAl_2O_4$ nanopowder (Aldrich) support were used in the preparations. In order to obtain the Ni core – Au shell structured nanoparticles, the Ni precursor was reduced first in the presence of stabilizing agents. The sol preparation method, that was successfully applied to get Au nanoparticles with size of the order of 6 nm [22] was modified for Ni, because tannin and

citrate reducing agents at the slightly basic pH used for preparation of gold sols were not strong enough to reduce Ni(II) nitrate. Thus, Ni nitrate solution in the presence of tannin and citrate at pH~5-6 was reduced with freshly prepared $NaBH_4$ solution at 60 ^oC. One min after the addition of the reducing agent a color change to deep brownish-grayish was observed, that turned a bit reddish when adding Au^{3+} ions after 9 min. Then fast fading of the liquid occurred with time and, after 1.5-2 hours, the monometallic Ni-containing sol became green, the bimetallic sol paled as well, meaning that oxidation and dissolution of Ni must have occurred. In order to avoid losing much of the nickel in solution the sol immobilization step was done within 1 hour after the reduction step. After 15 min at 60 ^oC sol adsorption onto the $MgAl_2O_4$ support was carried out with the aid of PDDA polycation as before in a previous study [22]. Samples were filtered, washed with water and dried at 80 ^oC for 48 hours. The notation and the exact concentrations of the final materials as determined by XRF and by Prompt Gamma Activation Analysis (PGAA) [23] are given in Table 1.

2.2. Sample characterization

The phase composition of crystalline components of fresh and calcined/reduced samples was investigated by X-ray diffraction (XRD) analyses. XRD patterns were recorded in Bragg-Brentano para-focusing geometry using a Bruker D5000 diffractometer, equipped with a Cu Kα anode and a graphite monochromator. The XRD data were collected in the angular range 10 - 70 ° in 2θ using 0.05 ° step size and counting time of 5 s per step. The assignment of the various crystalline phases was based on the JPDS powder diffraction file cards [24]. Mean crystallite sizes are calculated from the line broadening of the most intense reflection using the Scherrer equation [25].

The distribution of Ni (and Au) and the size of metal particles were studied by a conventional Philips CM20 transmission electron microscope (TEM) operating at 200 kV equipped with energy dispersive spectrometer (EDS) for electron probe microanalysis. The TEM samples were prepared by drop drying either the aqueous suspensions of the Au-Ni/$MgAl_2O_4$ samples or simply the sol on carbon-coated micro grids. The particle size distribution was obtained by measuring the diameter of equiaxial metal particles. High resolution transmission electron microscopy investigtions (HRTEM) and electron energy loss spectroscopy (EELS) elemental mapping were carried out by a JEOL 3010 microscope operating at 300 kV with point resolving power of 0.17 nm and a GATAN Tridiem Electron Energy Loss Spectrometer in the image filtering mode, respectively. Temperature programmed reduction (TPR) experiments were carried out with a Micromeritics Autochem 2910 apparatus equipped with a thermal conductivity detector (TCD). The gas mixture with composition 5% H_2 in Ar (50 mL/min) is used to reduce the samples (30 mg), heating from room temperature to 800 °C at the rate of 10 °C / min. Before starting the TPR analyses, the catalysts were pretreated with a flowing gas mixture of 5% O_2 in He (50 mL/min) at 550 ^oC for 30 min, then cooling down under Ar. The amount of carbon on the sample surface after catalytic run was estimated from the amount of CO_2 evolved in temperature programmed oxidation (TPO) experiments carried out in 10 vol. % O_2 and 1 vol.% Ar in He. Mass spectrometer was employed to detect CO_2 formation.

The X-ray photoelectron spectroscopy (XPS) analyses of the fresh and calcined/reduced catalysts were performed with a VG Microtech ESCA 3000 Multilab, equipped with a dual Mg/Al anode. The spectra were excited by the unmonochromatised Al Kα source (1486.6 eV) run at 14 kV and 15 mA. The analyzer operated in the constant analyser energy (CAE) mode. Survey spectra were measured at 50 eV pass energy. For the individual peak energy regions, a pass energy of 20 eV set across the hemispheres was used. The sample powders were mounted on a double-sided adhesive tape. When performing the analyses of reduced samples, particular

care was taken to minimize the exposure to the air by storing and then loading the samples under inert atmosphere using a glove box. The pressure in the analysis chamber was in the range of 10^{-8} Torr during data collection. The constant charging of the samples was corrected by referencing all the energies to the C 1s peak energy set at 285.1 eV, arising from adventitious carbon. The invariance of the peak shapes and widths at the beginning and at the end of the analyses ensured absence of differential charging. Analyses of the peaks were performed with the software provided by VG, based on non-linear least squares fitting program using a weighted sum of Lorentzian and Gaussian component curves after background subtraction according to Shirley and Sherwood [26-27]. Atomic concentrations were calculated from peak intensity using the sensitivity factors provided with the software. The binding energy values are quoted with a precision of ± 0.15 eV and the atomic percentage with a precision of ± 10%. XPS analyses were carried out also on the used catalysts.

2.3. Catalytic measurements

Before the catalytic measurements the just dried catalysts were calcined in 10% O_2/1% Ar/He in situ at 550 °C for 30 min to remove the carbonaceous contamination, then reduced in 20% H_2/He at 750 ^oC for 30 min. Catalytic reaction was performed using CH_4/CO_2/Ar = 69/30/1 mixture. It should be pointed out that the particular reagent gas mixture was chosen to mimic the composition of some natural gas wells in Hungary [13]. 30 mg of catalyst along with 30 mg of diluting quartz beads were tested in a quartz reactor where the reactant mixture at a flow rate of 20 ml/min was introduced. Temperature during the reaction was raised up to 850 ^oC with 10 C/min (standard reaction with temperature ramp). A quadrupole mass spectrometer was used for analysis of the reaction products. Ar was used as internal reference for calculation of the methane and carbon dioxide conversion values after adequate calibration. After the first catalytic run the samples underwent a regeneration step consisting of a TPO ramp to 750 ^oC with 30 min hold time, followed by cooling in Ar atmosphere, and then of a TPR rump to 750 ^oC with 10 ^oC/min and 30 min hold time. Thereafter a second catalytic run was performed. In order to check for time stability, new portion of the sample was pretreated (calcined and reduced) and contacted with the reactant mixtures as above, then the reaction temperature was increased to 650 °C with 10 ^oC/min and 20-24 h hold time. The conversions were monitored as function of time and the zero value on the time scale corresponded to the point when 650 ^oC was reached.

3. Results and Discussion

3.1. Genesis and structure of Au and Ni containing nanoparticles in the sol

The adopted particle synthesis procedure is somewhat similar to the spontaneous electroless deposition of a precious metal (Au) layer on Ni substrate immersed into a solution containing gold ions [28-30]. Surface replacement takes place spontaneously because of the difference in standard potentials of Ni(II)/Ni and Au(III)/Au couples. In our case, the H_2 evolved during the decomposition of $NaBH_4$ acted as extra reducing agent allowing for a fast and complete reduction of Au(III).

As mentioned above, judging from the color fading of the liquid, the monometallic colloidal nickel underwent significant dissolution into ionic nickel. The color change was less dramatic in the case of the AuNi samples suggesting that Ni oxidation and dissolution was to some extent prevented by Au coverage.

Since significant color change occurred during sol preparation and adsorption, TEM and HRTEM measurements of the monometallic Ni sol and of the bimetallic sol with the highest concentration of gold (Ni-3Au) were done to determine the size, arrangement and possibly the

structure of the bimetallic and/or monometallic particles in the liquid phase. In order to check for structural evolution, the measurements were taken after 2 different times during the reduction process. The TEM and HRTEM images of the parent Ni sol, 5 min after adding $NaBH_4$ are given in Fig. 1. Ni particles of ~ 12 nm in size visible in Fig. 1 A, according to the selected area electron diffraction pattern (SAED) in the inset, were amorphous. The formation of amorphous nickel particles was also reported in literature when using $NaBH_4$ as reducing agent [31]. In the panels B and C of the same figure the HRTEM and the corresponding Fast Fourier Transform (FFT) images are shown. Accordingly, the amorphous Ni containing particles had a crystalline outer shell formed by NiO, characterized by NiO(111) lattice fringes. The oxide shell could have been formed in air during sample transfer. Indeed after storage of the sample grid for 2 weeks in air the initially amorphous particles turned completely into crystalline NiO.

The TEM image of the Au containing sol sample, 12 min after the very start of reduction, is shown in Fig. 2A. Spherical amorphous particles of 10-18 nm, small individual crystalline particles of ~ 4-6 nm and aggregates of some smaller particles can be seen. As derived from EDS analysis, the composition of the particles was rather heterogeneous. The large amorphous particles were mainly constituted by Ni (92%), the small darker ones had an Au and Ni composition close to the bulk value and the large irregularly shaped or aggregated particles were more enriched in gold with respect to the bulk composition. TEM, HRTEM and FFT of a small 4-6 nm crystal in Fig. 2B show details of the structure of the sol particle. The particle is twinned and exhibits fringes identified by its lattice distance and symmetry as Au (111). The panel in Fig. 2C depicts the TEM image, Ni(855 eV) elemental map, B(188 eV) elemental map, HRTEM and FFT of a particle. The elemental maps indicate both a remarkable Ni and B content, at this stage of the synthesis. According to literature, Ni nanoparticles reduced by $NaBH_4$ may indeed contain some boron which after calcinations at relatively low temperature, above 250-300°C in air, is easily removed [32]. In our case the complete removal of boron after calcination and reduction treatment was ascertained by elemental mapping during HRTEM measurements.

To summarize, according to the TEM and HRTEM analyses, the adopted sol procedure allowed an intimate contact between Ni and Au, producing nanoparticles with different Ni/Au composition.

3.2. $MgAl_2O_4$ supported Au-Ni catalyst

As reported in Table 1, according to the elemental analysis, all the supported samples contained about 4 wt% of Ni. The loadings of gold agreed quite well with the nominal values and are reported in the sample notation.

TEM measurements were carried out on the as prepared samples (i.e. just dried). The TEM image in Fig. 3A refers to the dried Ni catalyst. The Ni or NiO particles can hardly be distinguished among the crystalline spinel $MgAl_2O_4$ support . EDS results were in accord with the analytical composition of Table 1. The panel in Fig. 3B refers to the dried Ni-3Au sample. In this case individual particles along with aggregates can be easily recognized. The EDS results confirmed an enrichment of gold in the large aggregates similarly to the corresponding sol.

The reducibility of the catalysts was investigated by temperature programmed reduction (TPR). Two cycles of TPR analysis were carried out. The first measurement (TPR1) was performed after oxidation at 550 °C corresponding to the initial calcination treatment before the catalytic reaction. A second measurement (TPR2) was performed after re-oxidation of the sample up to 750 °C in order to detect possible structural modification due to the thermal

treatment of a regeneration step applied between catalytic runs (see later). In Fig. 4 the TPR profiles are shown. The TPR1 patterns of the monometallic nickel and bimetallic Ni-Au samples were characterized by two peaks, one at ~ 350 °C and the other at ~ 600 °C. The presence of gold did not affect significantly the shape of the profiles. According to literature, the low temperature peak could be attributed to "free" NiO whereas the high temperature peak could correspond to Ni^{2+} species not completely integrated in the spinel structure of the support but with a certain degree of interaction [33]. The exact position of this second peak is related to the strength of interaction. Generally, larger particles would interact less with the support and would be easier to reduce, with a reduction peak shifted to lower temperature [34]. In the TPR2 curves, after the sample oxidation at 750 °C, the two peaks coalesced into one at 440 °C with the exception of the monometallic Ni sample which still presented two features much closer in temperature as compared to the TPR1. In this latter case, the lowering of the high temperature peak observed in the second TPR, according to literature, could be due to the high temperature sintering of the nickel particles over the support $MgAl_2O_4$ [35].
The presence of a single peak at the same temperature for all the gold containing samples reflected a more homogeneous chemical arrangement of the nickel oxide causing same reducibility for all the nickel.
In order to investigate size effects on the particle reducibility, metal particle size distribution were obtained from TEM analyses of the samples after the two TPR cycles. The corresponding curves are shown in Fig. 5. The invariance of the TPR2 patterns among the bimetallic samples, notwithstanding the differences in Fig. 5, suggested that the corresponding reduction peaks were likely related to the formation of a new alloy phase and did not depend on the particle size. On the contrary, in the case of the monometallic nickel sample, an increase of the crystallite size would justify the shift of the high temperature peak of TPR2 to a lower temperature as compared to TPR1.
The surface of the catalysts was analyzed by X-ray photoelectron spectroscopy. In order to investigate the surface modification upon the oxidation and reduction treatments, XPS measurements were done over the calcined and the reduced samples after the second TPR. In Table 2 the Ni $2p_{3/2}$ and Au $4f_{7/2}$ binding energies and the atomic ratio of the nickel over the support constituents Mg and Al and of Ni/Au are listed for the various catalysts in the two different states. The typical Ni 2p photoelectron spectra of the calcined and reduced samples are shown in Fig. 6 for the monometallic $Ni/MgAl_2O_4$ sample. In the figure the experimental and the curve fitted spectra are shown. The spectra were characterized by the two spin orbit components Ni $2p_{3/2}$ and Ni $2p_{1/2}$ separated by ~17-18 eV and by two shake up satellite peaks located at about 6 eV higher energy with respect to the main photoelectron peaks. The calcined samples exhibited the Ni $2p_{3/2}$ binding energy at 855.5 ± 0.2 typical of oxidized nickel with a spin-orbit coupling energy gap of ~18.1 eV [36]. Pure NiO is generally characterized by a Ni $2p_{3/2}$ binding energy of 854.5 eV. The value obtained in the present samples was intermediate between the bulk NiO and the spinel $NiAl_2O_4$ or the NiO-MgO compound both exhibiting Ni $2p_{3/2}$ binding energies of ~ 856 eV [37-38]. Therefore a chemical interaction between nickel and $MgAl_2O_4$ support, in accord with the TPR results, could be the reason for the observed energy value. After the two TPR cycles, the Ni 2p peaks were split into two components, one at lower energy ~ 852.4 ± 0.2 eV proper of metallic nickel and the other at higher energy typical of the oxidized nickel [36]. As shown in Table 2, contrary to what is generally expected from a metal impregnation procedure, the XPS derived Ni/(Mg+Al) atomic ratios were rather comparable with the corresponding analytical ratio of 0.1 indicative of a homogeneous composition. According to the XPS analyses of the samples, after the second TPR a significant reduction of the Ni/Au atomic ratio was observed. Such change may reflect either a decrease of

the surface nickel content due to an increase of the nickel particle size, either an inward diffusion of nickel, either coverage of the nickel particle by another chemical species. With respect to the gold, unfortunately the Au $4f_{5/2}$ component overlapped with the Mg 2s peak of the support. However through a curve fitting procedure, on the bases of the bare Au $4f_{7/2}$ component, by constraining the position, the line width and the intensity of the $4f_{5/2}$ component with respect to the $4f_{7/2}$, it was possible to obtain the complete Au 4f spectra as given in Fig. 7 for the Ni-3Au sample after calcination and after TPR treatments. The binding energy values of the Au $4f_{7/2}$ reported in Table 2 were typical of metallic gold. The negative shift of about 0.7 eV between the Au $4f_{7/2}$ values of the calcined samples and the reduced samples although affected by a large uncertainty of the peak position of the former samples, could reflect a real electron deficiency of gold in the calcined sample where the noble metal was likely embedded in the support. Indeed, as suggested by the decrease of the Ni/Au atomic ratio and by the corresponding increase of the Au $4f_{7/2}$ intensity peak as compared to the support Mg 2s peak, clearly shown in Fig. 7, the reduction treatment drove gold to the surface where it became definitely metallic. Moreover, according to literature the formation of an Au-Ni alloy, would produce an Au $4f_{7/2}$ positive shift of around 0.48 eV for Au diluted in bulk nickel and a Ni $2p_{3/2}$ shift of -0.70 eV for nickel diluted in bulk gold [39]. In the present case, the Au $4f_{7/2}$ energy shift in the reduced samples as compared to the calcined ones was in the opposite direction. The coexisting presence of two different alloys, revealed by the XRD patterns (see later), one diluted and the other enriched in gold may result in the un-shifted binding energy of 83.6 eV typical of pure gold. The same argument is applicable to the Ni 2p binding energy. It is worth saying that XPS analyses (spectra not shown here) of the selected Ni-3Au sample after the consecutive TPR/TPO treatments yielded a value of the atomic Ni/Au ratio comparable to the one obtained after the initial calcination. Moreover, to check the surface composition of the catalysts just before the reaction, the Ni-3Au sample was analysed right after the hydrogen reduction pretreatment. The obtained Ni/Au atomic ratio was again much smaller as compared to the calcined and to the TPR/TPO treated sample and quite similar to the value obtained after the two consecutive TPR treatments. The results of the XPS analyses confirmed that the Ni-Au bimetallic samples underwent chemical compositional changes upon exposure to different environments at high temperature. In other words the reducing atmosphere caused the surface segregation of gold, whereas the oxidative atmosphere induced de-alloying and/or nickel surface segregation.

XRD investigations of the samples in the different stages of their life were performed. Unfortunately the significant overlap of the $MgAl_2O_4$ support peaks with those from gold and nickel present in the sample hindered the proper analyses of the metal peaks providing particle sizes. The XRD patterns of the monometallic Ni sample, not shown here for brevity, were characterized only by the support peaks. No significant changes were observed in the pattern of the reduced sample with respect to the calcined one, at exception of a worse signal to noise ratio probably due to the scanty amount of sample collected from the TPR reactor. The calcined gold containing samples were characterized by similar patterns. Only some meaningful information was obtained from the pattern of the higher gold content sample Ni-3Au, exhibiting the main Au (111) peak. In Fig. 8 the XRD patterns of this sample after the different treatments are shown. Quite interesting, after the TPR1, the Au (111) was shifted to higher angles whereas the position of the Ni (111), previously hidden by the spinel peak, was appearing at a lower angle with respect to the Ni bulk position [24]. Such observation was indicative of AuNi alloy formation. According to the Vegard's law the shifts of the metal peaks in the bimetallic sample with respect to the pure metal position are indicative of alloy formation and can be used to estimate the composition of the alloy [25]. From the differences of the lattice parameters, obtained from the Au (111) and Ni (111) peaks, the composition of

two alloy phases, one enriched in gold and the other enriched in nickel were approximately estimated. After the oxidation during the TPO, the gold peak moved back to the pure metal peak position. Moreover, the Ni alloy peak disappeared and two new features due to NiO (200) and NiO (220) were observed. A reversible structural change occurred after TPR2 producing again the AuNi alloys and disappearance of the NiO phase. The two different alloys may be present as separate particles or could be present in the same particle of different layer composition. The HRTEM of the sample after TPR2, shown in Fig. 9 confirmed the latter assumption derived from the XRD and XPS analyses, with particles composed of an alloy core enriched in nickel and an alloy shell enriched in gold. According to the literature, large miscibility gap exists in the phase diagram of Au-Ni system. There is a mutual solubility in the solid state above ~ 800 ^{o}C for all composition of the two metals, but at low temperature two distinct phases (rich in Au and rich in Ni) form, whose composition depends on the two metal relative concentration, the temperature and the cooling rate [40]. Despite the theoretical immiscibility of the two bulk metals at low temperatures, we can find several examples about the successful preparation of nanosize AuNi alloy particles [41, 42, 43]. Our structural results revealed that metal particles containing different amount of gold and nickel are very sensitive to the changes of temperature and gas atmosphere. Monte Carlo simulations [44] confirmed the de-alloying in an immiscible Au/Ni(110) system: after a certain number of Au monolayer, with further increase in Au content, the number of alloying Au atoms decreases. Furthermore, with increase in temperature the number of alloying atoms increases up to saturation at about 530 ^{o}C, while at about 630 ^{o}C, the number of surface Ni atoms jumps to a very high value indicating a structural change of the surface. AES measurements also showed that with 0.4 ML Au coverage on Ni(111), at 580-630^{o}C Au starts to diffuse into the bulk and at 1000 ^{o}C it completely disappears from the surface [45]. Such complex structural changes have to be kept in mind when analysing the catalytic behaviour of the Au-Ni bimetallic system used in dry reforming reaction, ramping the temperature up to 800 ^{o}C.

3.3. Catalytic behavior

Catalytic activity of the samples was measured first as a function of temperature. In the case of the pure nickel sample and the 0.5wt% Au containing catalyst, the conversion curves were rather similar and as shown in Fig.10 the reaction started at around 400 °C with the conversion gradually rising with temperature. The addition of increasing amount of gold induced a shift in the starting temperature to 500 °C followed by an activation step and an abrupt increase of the conversion. Then an improvement of the activity was observed with the complete conversion of CO_2 and the highest conversion of CH_4 occurring at lower temperature as compared to the pure nickel catalyst. The high methane conversion may be due to some parallel reactions such as decomposition of methane or steam reforming of methane with the water produced by the reverse water gas shift reaction, favored at the high temperature. The sudden rising of the conversion curves after a sort of plateau, observed for the bimetallic catalysts, implied a period of catalyst activation. Similar behavior was observed with impregnated supported nickel catalysts [13]. However in that case, in the absence of any reduction pretreatment, the induction period corresponded to the time needed for the reduction of NiO by methane or by the hydrogen produced by methane decomposition at higher temperature [13]. In the present case, the formation, during reducing conditions, of an AuNi alloy with surface gold enrichment, as proved by XRD and XPS analyses, would likely reduce the amount of exposed nickel active sites, therefore retarding the catalytic conversion. Moreover according to DFT calculations, the replacement of surface nickel atoms by gold atoms would increase the dissociation barrier for the CH_4 over Ni atoms whereas dissociation

over the Au atoms is expected to have a much higher energy barrier [21, 45-46]. The temperature delay in the beginning of the reaction, occurring at 500 °C, as seen in Fig. 10, may therefore be explained by this increase in the methane dissociation barrier due to gold. Since we have used unusual composition of CH_4 and CO_2 and not the stochiometric ratio of 1:1, the high probability of surface coke formation have to be seriously considered. It is widely accepted in studies about thermodynamic analysis of dry reforming, that the methane decomposition reaction is the main reason for the significant increase of methane conversion at high temperatures. When CO_2/CH_4 ratio = 0.5 (such as about in our case), CO_2 gas acts as limiting reactant and the RWGS reaction is not favored along with dry reforming reaction at higher temperatures [47]. Therefore, high conversion of CH_4 at higher temperature can be ascribed to methane decomposition to form large amount of H_2 and surface carbon. A thermodynamic equilibrium analysis of the multireaction system for the CO_2 dry reforming of methane was performed by Amin et al. considering different CO_2/CH_4 ratios [47]. In correspondence of CO_2/CH_4 = 0.5, including methane decomposition in their calculations, the authors obtained simulated CH_4 conversion (at 800^{o}C ~95%), higher than what reported in previous studies for the same reagent ratio. In our case thermodynamic equilibrium calculations were also carried out, with and without considering surface carbon as stable compound, by HSC Chemistry program. Observed discrepancies between the calculations and the experimental data were attributed to the neglecting of the H_2O detection during the catalytic run. All in all, calculated equilibrium concentrations of CH_4 and CO_2 at 800 ^{o}C without considering carbon were 25% and 0 mol%, respectively, while the present corresponding experimental data obtained on Ni sample were 18 mol% CH_4 and 0 mol% CO_2. However, when one considers surface carbon, C(s) in equilibrium (since our conditions allow this), the calculated equilibrium CH_4 concentration decreases to 0 mol% with large amount of H_2 produced (52 mol%H_2). At lower temperatures even the calculations without considering carbon fit the experimental data showing that the experimental measurements were within the corresponding thermodynamic limits.

To check for the catalyst reusability a second catalytic run was performed after a regeneration step consisting of a TPO ramp up to 750 °C with a hold time of 30 min followed by a reduction at 750 °C with 10 ^{o}C/min rate and hold time of 30 min. A comparison of the first and second runs for the monometallic Ni and the bimetallic Ni-3Au catalysts is given in Fig. 11. The corresponding CO/H_2 ratios at the different temperatures are also plotted. For the sake of clarity only the data obtained above 520 °C, at which temperature the bimetallic exhibited significant activities, are shown. The curves of the two catalytic runs in the case of the monometallic Ni sample were rather reproducible. On the contrary, the bimetallic catalyst in the second catalytic run deactivated a little. The activation step observed in the first run was still present in the second run. Mostly interesting the variations of the CO/H_2 ratio as a function of temperature were different for the mono and the bi-metallic catalysts. First of all, the gold containing sample was characterized by a much higher ratio (more than double) with respect to the theoretical value of 1 in the temperature range of the induction period where the conversions were low. With the increase of the temperature and increase of the methane and CO_2 conversion the CO/H_2 ratio lowered down to a value of 0.7. The monometallic sample exhibited a CO/H_2 ratio closer to 1 which slightly decreased with the conversion at the higher temperatures. These variations were in accord with the occurrence of parallel reactions, in particular a high CO/H_2 ratio could be the outcome of the reverse water gas shift (RWGS) reaction between the unreacted CO_2 and the hydrogen, being catalysed by gold [48]. At increasing temperature the water evolved during the RWGS will react with methane by steam reforming producing an excess of hydrogen and therefore decreasing the CO/H_2 ratio. It is

worth noticing that whereas in the case of the monometallic nickel catalyst, the curves of CO/H_2 ratio of the two runs were rather similar, in the case of the bimetallic sample larger values of the CO/H_2 were observed in the 500°C -700°C range of the second run. This could be indicative of surface gold segregation and of a structural rearrangement during the thermal treatments in oxygen and hydrogen, as suggested by the TPR results described above. Such surface rearrangement could be the origin for the slight deactivation of the bimetallic catalyst observed in the second run.

The stability of the catalysts was checked during a long term reaction run at 650 °C. In Fig. 12 the CH_4 and the CO_2 conversion curves along with the CO/H_2 ratios as function of time are shown for the two selected samples, the Ni and the Ni-3Au. At the beginning of the run the two catalysts had similar conversions. However, whereas the monometallic Ni after a slight initial deactivation maintained a stable performance in terms of both methane and CO_2 conversions, the gold containing catalyst behaved like the monometallic with respect to the methane conversion, but it seemed to deactivate more with respect to the CO_2 conversion. The aging of the bimetallic catalyst affecting more the RWGS reaction than the DRM reaction could justify this behavior and it could also account for the similar ratio $CO/H_2 \sim 1$ obtained for both catalysts.

Carbon deposits produced during the reaction were detected by TEM measurements carried out on the samples after the second catalytic run. The TEM image of the aged Ni-0.45 Au sample (after the second catalytic run), given in Fig. 13 was typical of all the analysed samples, monometallic and bimetallic ones. Carbon was present as encapsulating graphite and nanotubes. Larger metal particles about 20-25 nm containing mainly Ni and some traces of Au were seen, either inside carbon nanotubes or surrounded by a graphite shell, whereas small ($d < 10$ nm) metal particles (Ni, Au, or NiAu) were located on the support. As seen from the particle size values listed in Table 1, in the presence of gold larger particles were formed after the reaction, in accord with the arrangement observed already in the sol.

In order to evaluate the carbon deposition on the catalyst surface, TPO measurements were carried out after reaction. The TPO curves obtained from the Ni and the Ni-3Au samples, after the first catalytic run, in terms of evolved CO_2 versus temperature are shown in Fig. 14. They were characterized by one broad CO_2 desorption peak centered at ~ 600 °C and at ~ 630 °C for the monometallic and bimetallic samples, respectively. The differences in the TPO peak maxima of the monometallic and bimetallic samples reflected a stronger bond between the carbon and the surface of the AuNi catalyst as compared to the nickel catalyst. Moreover, in spite of being a little more difficult to remove, the amount of carbon formed on the bimetallic sample with 3wt% Au was less (about 3 mg) than the amount formed on the monometallic catalyst (4 mg).

These results confirmed that the addition of gold to the $MgAl_2O_4$ supported Ni catalysts, under the conditions of methane reforming with CO_2, slightly hindered the removal of the carbon deposit, in accord with recent literature on Ni catalyst supported on alumina [10], but overall at the end of the reaction at 800 °C, produced less deactivating coke in accord with a previous study [13]. Probably the dilution of the nickel ensemble and the preferential adsorption of the gold atoms at the Ni step sites, being the nucleation sites for the carbon [14], would inhibit the formation of large coke molecules and could explain the slight improvement in the catalyst activity of the bimetallic as compared to the monometallic nickel catalyst, at higher temperatures.

4. Conclusion

The preparation of $MgAl_2O_4$ supported nickel nanoparticles doped with gold from metal

sol deposition allowed to obtain highly dispersed catalysts with variable particle composition. The intimate contact of gold and nickel was demonstrated by electron microscopy investigations. According to XPS, TPR and XRD analyses, structural modification of the catalysts occurred at different stages of the catalyst life.. After the reduction at high temperature both gold and nickel enriched alloyed particles were formed. An increase of the DRM activity at the temperatures between 700-800 °C was observed for the higher gold loaded catalysts (1.5 and 3 wt%) as compared to the monometallic Ni catalyst during temperature ramped reaction. However, the slightly poorer activity of the bimetallic catalysts observed at lower temperature was attributed to the formation of the less active AuNi alloy phase. The study justified the ambiguity existing in literature about the gold effect on the nickel catalyst. Indeed gold appeared to play a twofold role. According to the TPO pattern after reaction, gold lowered the amount of formed carbon during the DRM reaction, but it increased the interaction between the carbon and the catalyst.

Acknowledgments

The authors are indebted for financial support of Erachemistry and the Hungarian National Research Fund (OTKA NN#107170). The Bilateral Collaboration Program supported by CNR and HAS is kindly acknowledged. The authors thank CNR and MIUR for financial support through project EFOR "Progetti CNR per il Mezzogiorno". The PGGA (prompt gamma activation analysis) measurements to Dr. Zsolt Kasztovszky (Centre for Energy Research, HAS) and the XRD measurements to Dr. Francesco Giordano from ISMN are gratefully acknowledged, too. We are indebted to Yu Lou at the Technical University of Munich for the thermodynamic equilibrium calculations.

References

1. J. F. Munera, S. Irusta L.M. Cornaglia, E. A. Lombardo, D. V. Cesar, M. Schmal, J. Catal. 245 (2007) 25-34.
2. M-S. Fan, A. Z. 2.Abdullah, S. Bhatia, ChemSusChem 4 (2011) 1643-1653.
3. J. Newnham, K. Mantri, M. H. Amin, J. Tardio, S.K. Bhargava, Int. J. of Hydrogen Energy 37 (2012) 1454-1464.
4. K. Tomishige, K. Fujimoto, Catal. Survey from Japan 2 (1998) 3-15.
5. M. Garcia-Dieguez, I.S. Pieta, M. C. Herrera, M. A. Larrubia, L. J. Alemany, G. Busca, J. Catal. 270 (2010) 136-145.
6. R. Rostrup-Nielsen. Catal. Today 18 (1993) 305-324.
7. N. Wang, W. Chu, T. Zhang, X. S. Zhao, Int. J. Hydrogen Energy 37 (2012) 19-30.
8. H. Eltejaei, H. R. Bozorgzadeh, J. Towfighi, M. R. Omidkhan, M. Rezaei, R. Zanganeh, A. Zamaniyan, A. Z. Ghalam, Int. J. Hydrogen Energy 37 (2012) 4107-4118.
9. A. Kambolis, H. Matralis, A. Trovarelli, Ch. Papadopoulou, Appl. Catal. A 377 (2010) 16-26.
10. I. P. Silverwood, N. G. Hamilton, A. R. McFarlane, J. Kapitan, L. Hecht, E. L. Norris, R. M. Ormerod, C. D. Frost, S. F. Partker, D. Lennon, Phys. Chem. Chem. Phys. 14 (2012) 15214-1525.
11. S. Ozkara-Aydinoglu, A. Erhan Aksoylu, Int. J. Hydrogen Energy 36 (2011) 2950-2959.
12. A. L. Pinheiro, A. N. Pinheiro, A. Valentini, J. M. Filho, F. F. de Sousa, J. R. de Sousa, M. G. C. Roha, P. Bargiela, A. C. Oliveira, Catal. Comm. 11 (2009) 11-14.

13. L. Guczi, G. Stefler, O. Geszti, I. Sajó, Z. Pászti, A. Tompos and Z. Schay, Appl. Catal., 375 (2010) 236–246.
14. H. S. Bengaard, J. K. Norskov, J. Sehested, B. S. Clausen, L.P. Nielsen, A.M. Molenbroek, J.R. Rostrup-Nielsen, J. Catal., 209 (2002) 365–384.
15. X-Y. Quek, D. Liu, W.N.E. Cheo, H. Wang, Y.Chen, Y. Yang, Appl. Catal. B 95 (2010) 374-382.
16. J. Guo, H. Lou, X. Zheng, Carbon 45 (2007) 1314-1321.
17. M.A. Ocsachoque, C. E. Quincoces, M. G. Gonzales, Stud. Surf. Sci. Catal. 167 (2007) 397.
18. M.A. Ocsachoque, F. Pompeo, G. Gonzales, Catal. Today, 172 (2011) 226-231.
19. B. Pawelec, S. Damyanova, K. Arishtirova, J.L.G. Fierro, L. Petrov, Appl. Catal. A, 323 (2007)188-201.
20. Y.-H. Chin, D.L. King, H.-S. Roh, Y. Wang, S.M. Heald, J. Catal., 244 (2006) 153–162.
21. F. Besenbacher, I. Chorkendorff, B. S. Clausen, B. Hammer, A. M. Molenbroek, J. K. Norskov, I. Stensgaard,

Science 279 (1998) 1913-1915
22. A.M. Venezia, F. L. Liotta, G. Pantaleo, A. Beck, A. Horvath, O. Geszti, A. Kocsonya, L. Guczi, Appl. Catal. A, 310 (2006)114-121.
23. T. Korányi, A. E. Coumans, E. J. M. Hensen, R. Ryoo, H. S. Kim, É. Pfeifer, Zs. Kasztovszky, Applied Catalysis A 365 (2009) 48-54.
24. JCPDS Powder Diffraction File Int. Centre for Diffraction Data, Swarthmore, 1989; File No. 42-1467.
25. Klug, H. P., and Alexander , L. E., "X-ray Diffraction Procedures for Polycrystalline and Amorphous Materials." Wiley, New York, 1954.
26. D.A. Shirley, Phys. Rev. B 5 (1972) 4709-4714.
27. P.M.A. Sherwood, in: D. Briggs, M.P. Seah (Eds.), Practical Surface Analysis, Wiley, New York, 1990, p. 181.
28. Y. S. Won, S. S. Park, J. Lee, J.-Y. Kim, S.-J. Lee, Appl. Surf. Sci. 257 (2010) 56-61.
29. A. Tegou, S. Armyanov, E. Valova, O. Steenhaut, A. Hubin, G. Kokkinidis, S. Sotiropoulus, J. Electroanal. Chem. 634 (2009) 104-110.
30. S. Papadimitiou, A. Tegou, E. Pavlidou, S. Armyanov, E. Valova, G. Kokkinidis, S. Sotiropoulus, Electrochim. Acta 53 (2008) 6559-6567.
31. D. Gozzi, A. Latini, G. Capannelli, F. Canepa, M. Napoletano, M.R. Cimberle, M. Tropeano, J. Alloys and Compounds 419 (2006) 32-29.
32. S-J. Chiang, B-J. Liaw, Y-Z. Chen, Appl. Catal. A, 319(2007) 144-152.
33. J. Guo, H. Lou, H. Zhao, D. Chai, X. Zheng, Appl. Catal. A, 273 (2004) 75-82.
34. L. Xu, H. Song, L. Chou, Appl. Catal. B, 108-109 (2011) 177-190.
35. S. R. Challa, A. T. Delariva, T. W. Hansen, S. Helveg, J. Sehested, P. L. Hansen, F. Garzon, A. Datye, J. Am. Chem. Soc. 133 (2011) 20672-20675.
36. S. Velu, K. Suzuki, M. Vijayari, S. Barman, C. S. Gopinath, Appl. Catal. B, 55 (2005) 1393.
37. B.W.Hoffer, A.D. van Langeveld, J.P. Janssens, R.L.C. Bonnè, C.M. Lok, J.A. Moulijin J. Catal. 192 (2000) 432-440.
38. E. Ruckenstein, Y. H. Hu, Appl. Catal. A, 183 (1999) 85-92.
39. J. L. Rousset, F. J. Cadete Santos Aires, B. R. Sekhar, P. Melinon, B. Prevel, M. Pellarin, J. Phys. Chem. B 2000, 104, 5430-5435.
40. M. Rodríguez-Rodríguez, J. L. Phase Transitions, 2 (1982) 241-246
41. S. Zhou, Z. Ma, H. Yin, Z. Wu, B. Eichhorn, S. H. Overbury, S. Dai, J. Phys. Chem. C 113 (2009) 5758-5765
42. I.-C. Chiang, Y.-T. Chen, D.-H. Chen, J. All. Comp. 468 (2009) 237-245
43. C.-C. Kim, C. Wang, Y.-C. Yang, Y.-K. Hwu, S.-K. Seol, Y.-B. Kwon, C.-H. Chen, H.-W. Liou, H.-M. Lin, G. Margaritondo, J.-H. Je, Mat. Chem. Phys. 100 (2006) 292-295.
44. W. Fan, X. G. Gong, Surf. Sci. 562 (2004) 219-225
45. P. M. Holmblad, J. Hvolbaek Larsen, I. Chorkendorff, J. Chem. Phys. 104 (1996) 7289-7295.
46. B. Hammer, J. K. Norskov, Nature 376 (1995) 238.
47. M. Khoshtinat Nikoo, N. A. S. Amin, Fuel Proc. Techn. 92 (2011) 678-691.
48. D. Andreeva, V. Idakiev, T. Tabakova, L. Ilieva, P. Falaras, A. Bourlinos, A.Travlos, Catal. Today 72 (2002) 51–57.

Figure 1. TEM (A), HRTEM (B) and FFT (C) images of the parent Ni sol 5 min after adding $NaBH_4$.

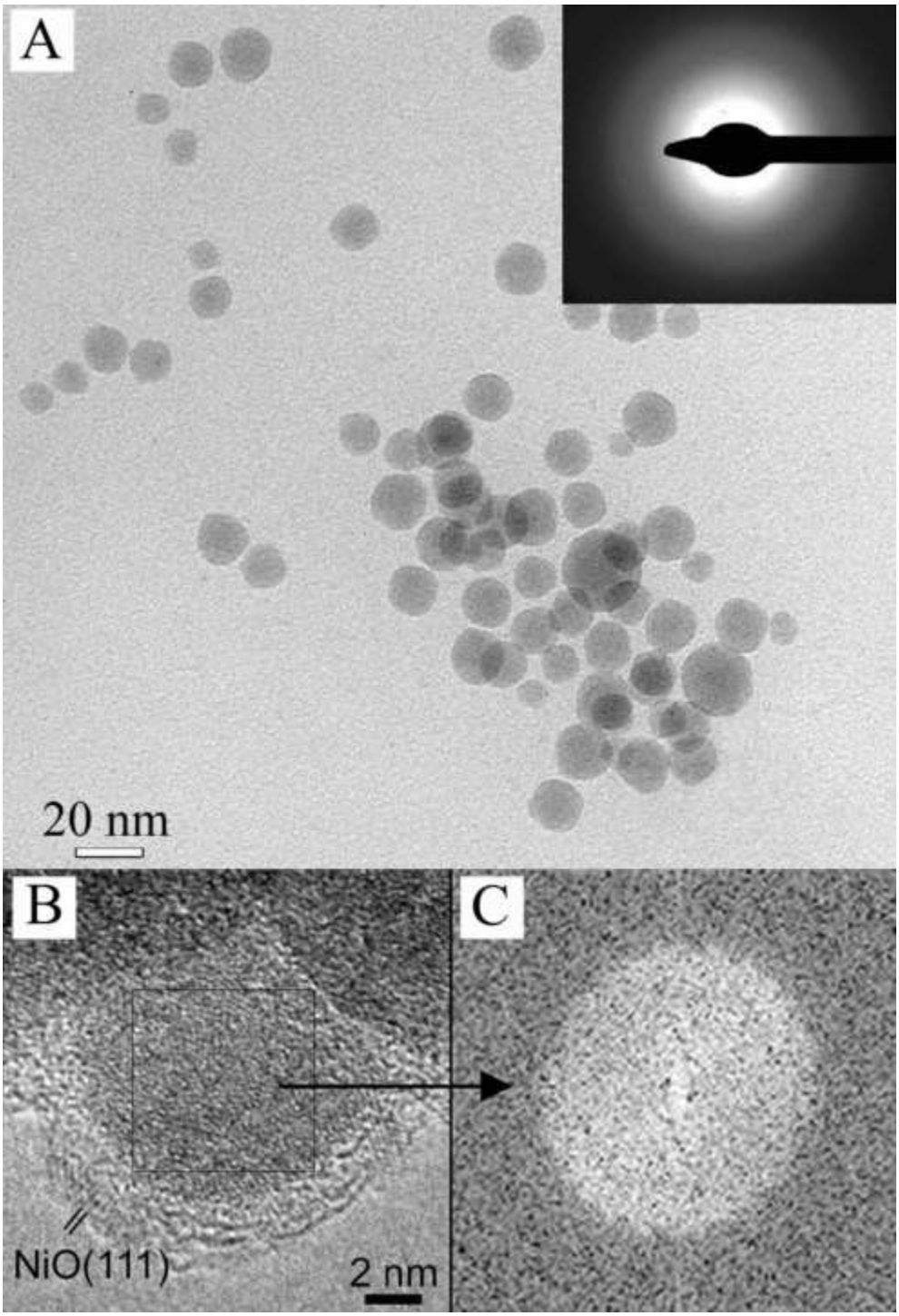

Figure 2. (A) TEM with EDS (measured places marked by circles), (B) HRTEM with FFT images of the Ni-3Au sol sample, 12 min after the start of reduction. The panels in C depict the TEM image, Ni(855eV) map, B(188eV) map, HRTEM and FFT of a particle, respectively.

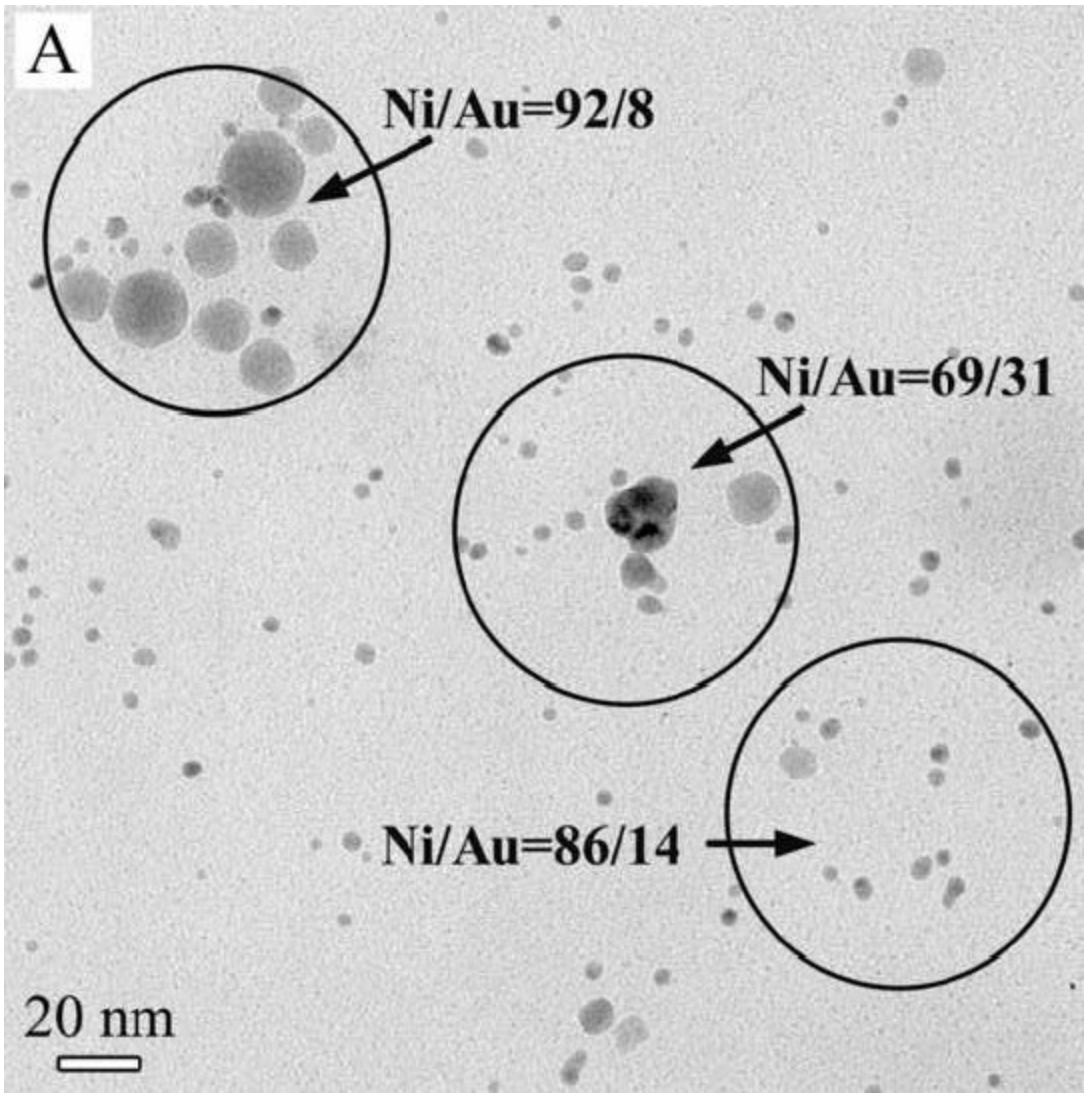

2a

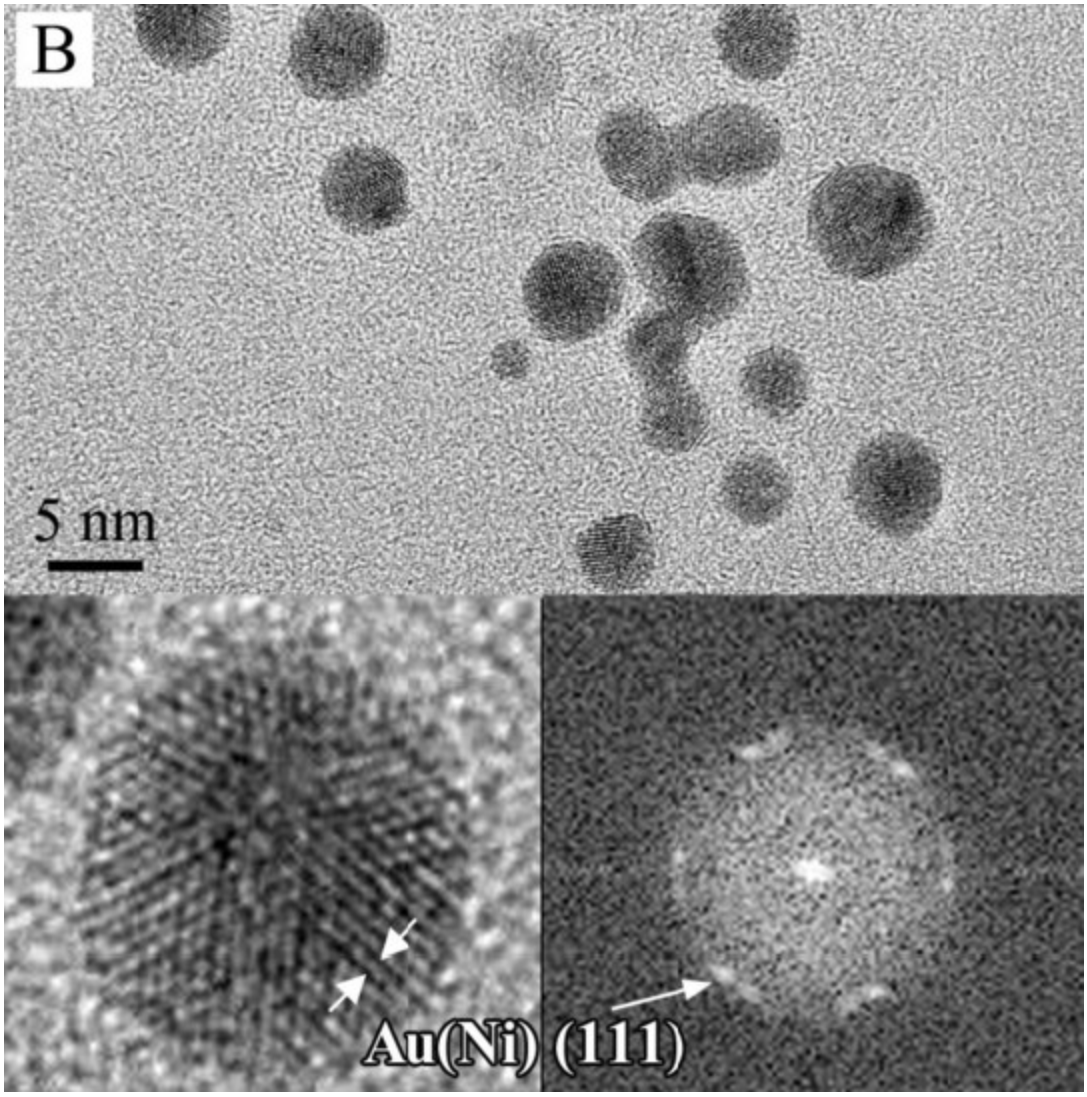

2b

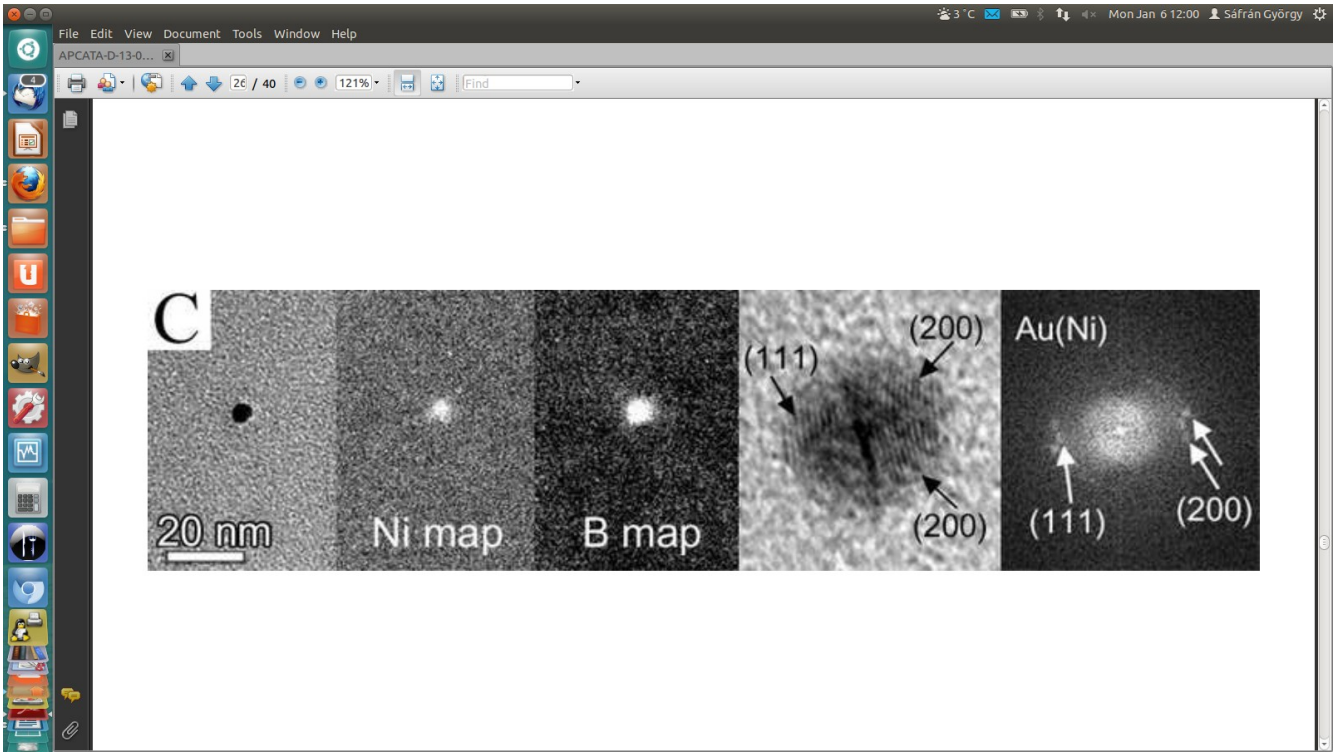
File Edit View Document Tools Window Help
APCATA-D-13-0...
2 / 40
121%
Find
C
20 nm
Ni map
B map
(111)
(200)
(200)
Au(Ni)
(111)
(200)

2c

Figure 3. TEM images and EDS data of as just dried catalysts: A) Ni; B) Ni-3Au (EDS refers to the circled area).

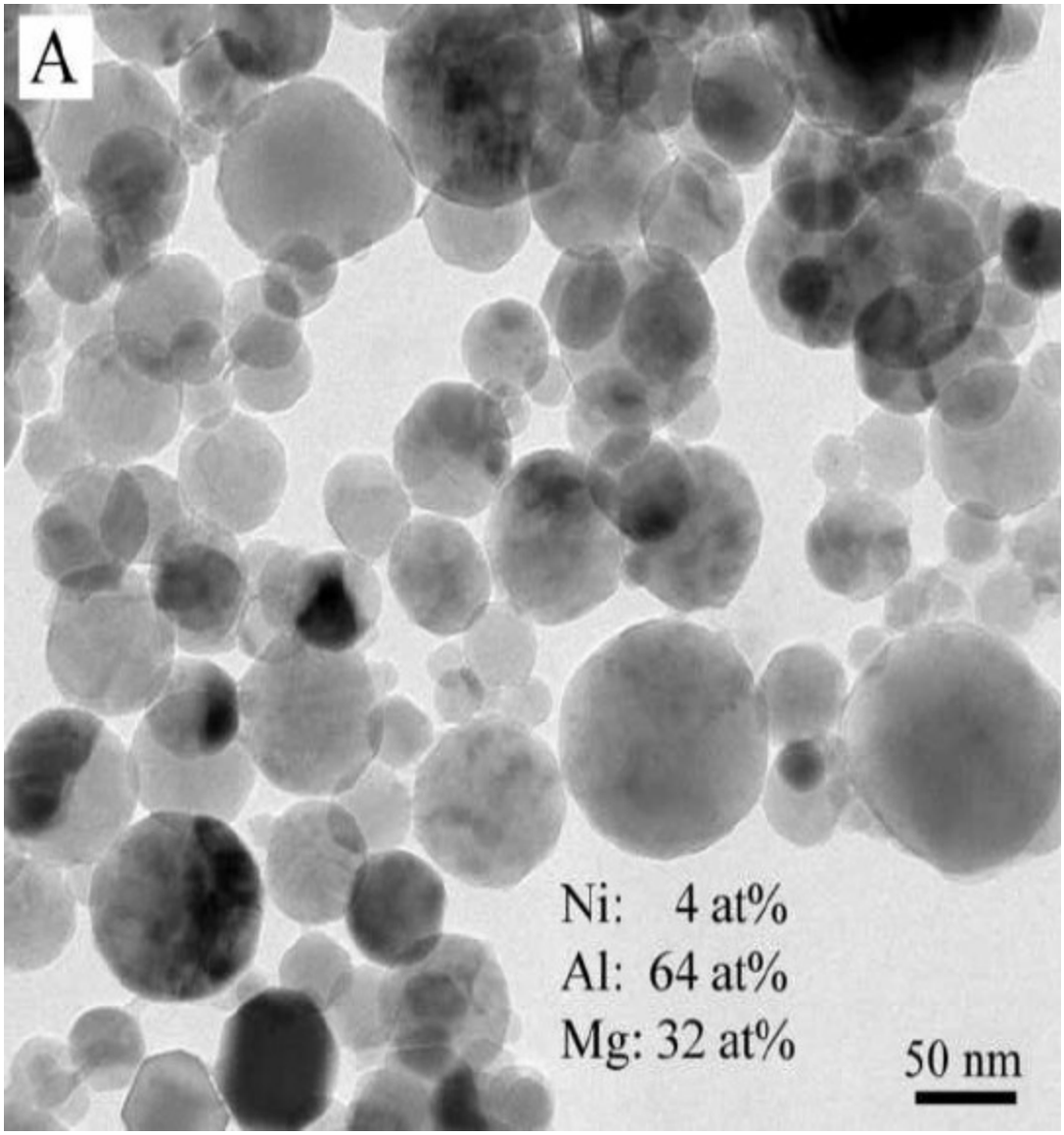

3a

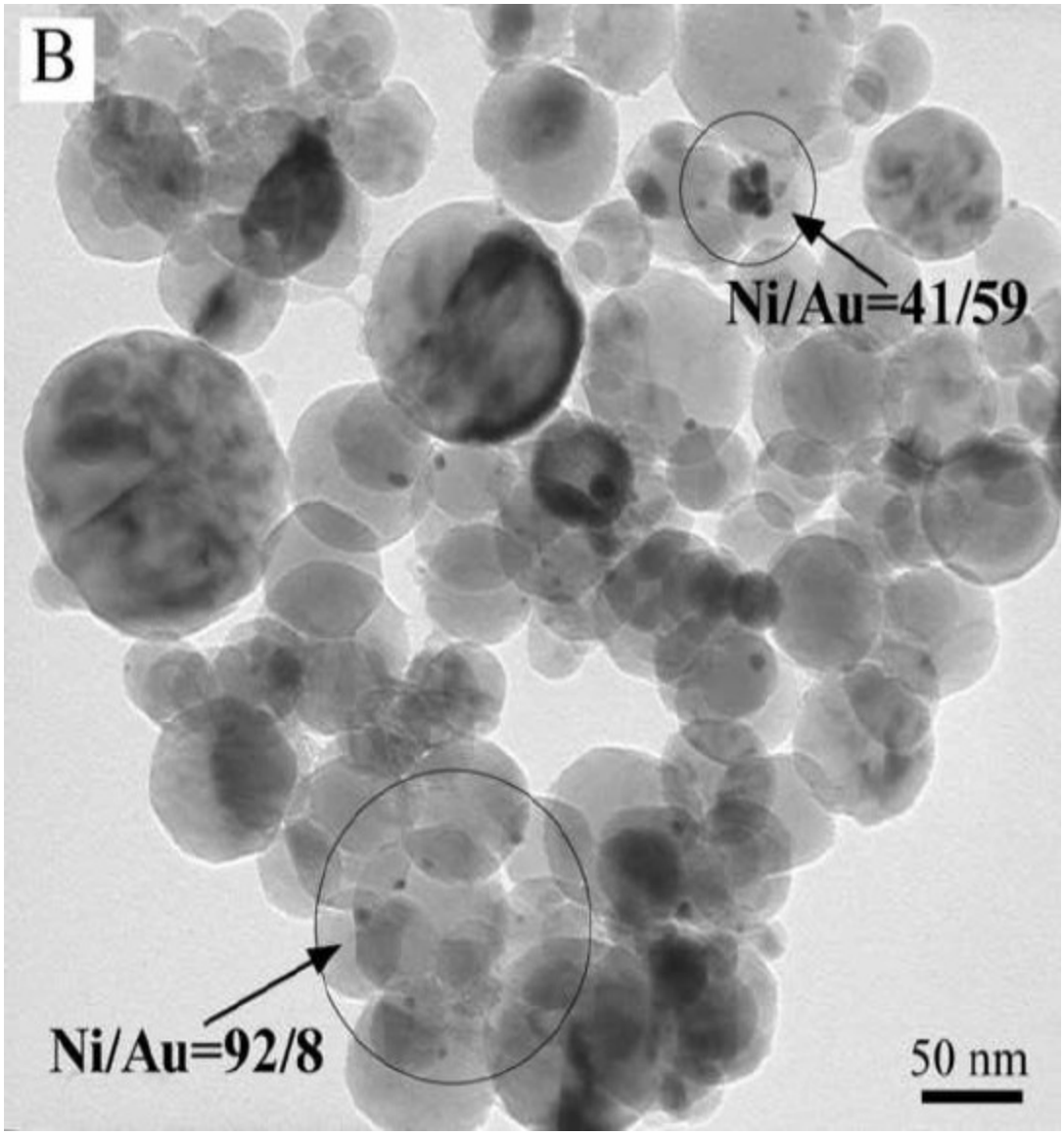

3b

Figure 4. TPR profile of the catalysts: a) Ni; b) Ni-0.5Au; c) Ni-1.4Au; d) Ni-3Au. Continuous and dashed curves correspond to the TPR1 and TPR2 runs respectively.

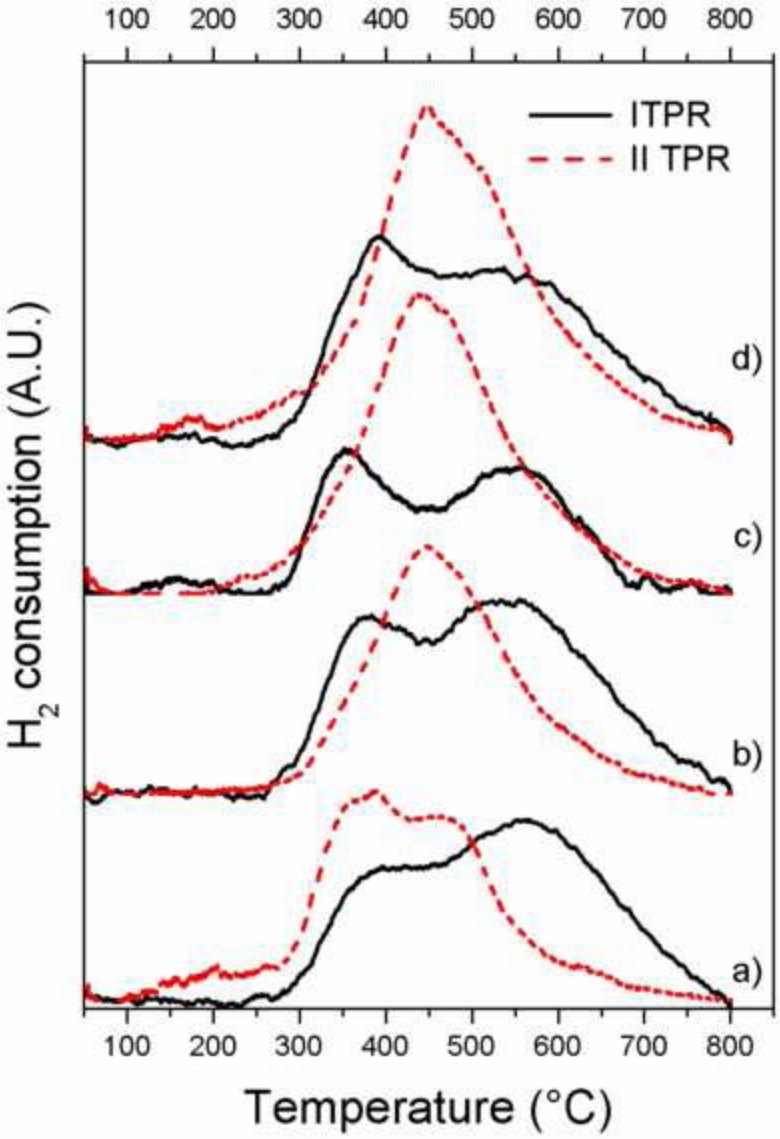

Figure 5. Particle size distribution determined by TEM after the second TPR.

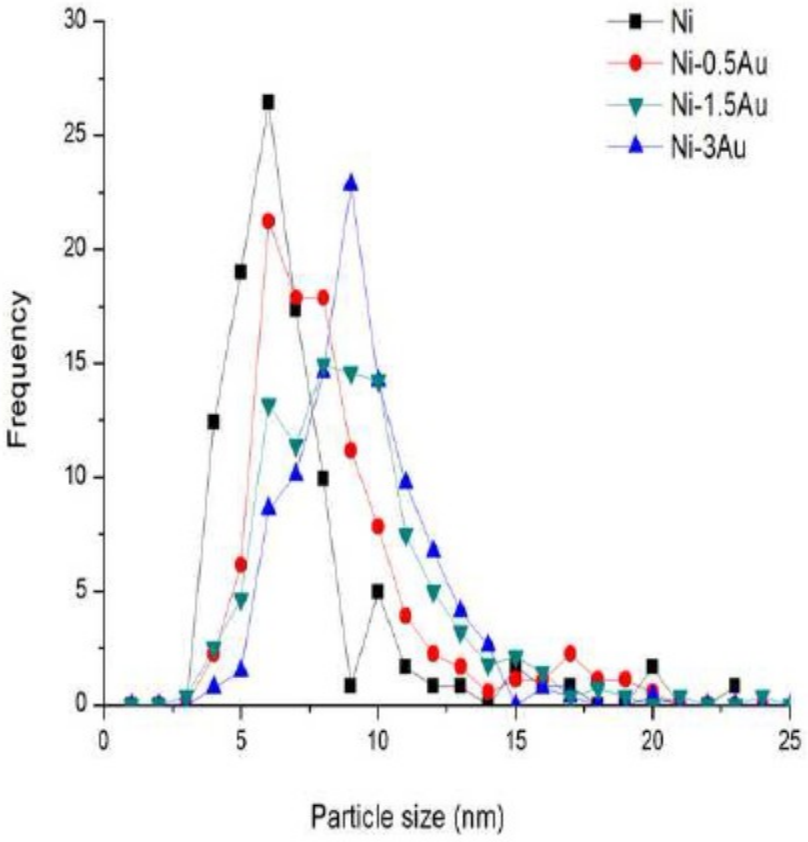

Figure 6. Ni 2p XP spectra of Ni catalyst: (a) as calcined, (b) after the second TPR.

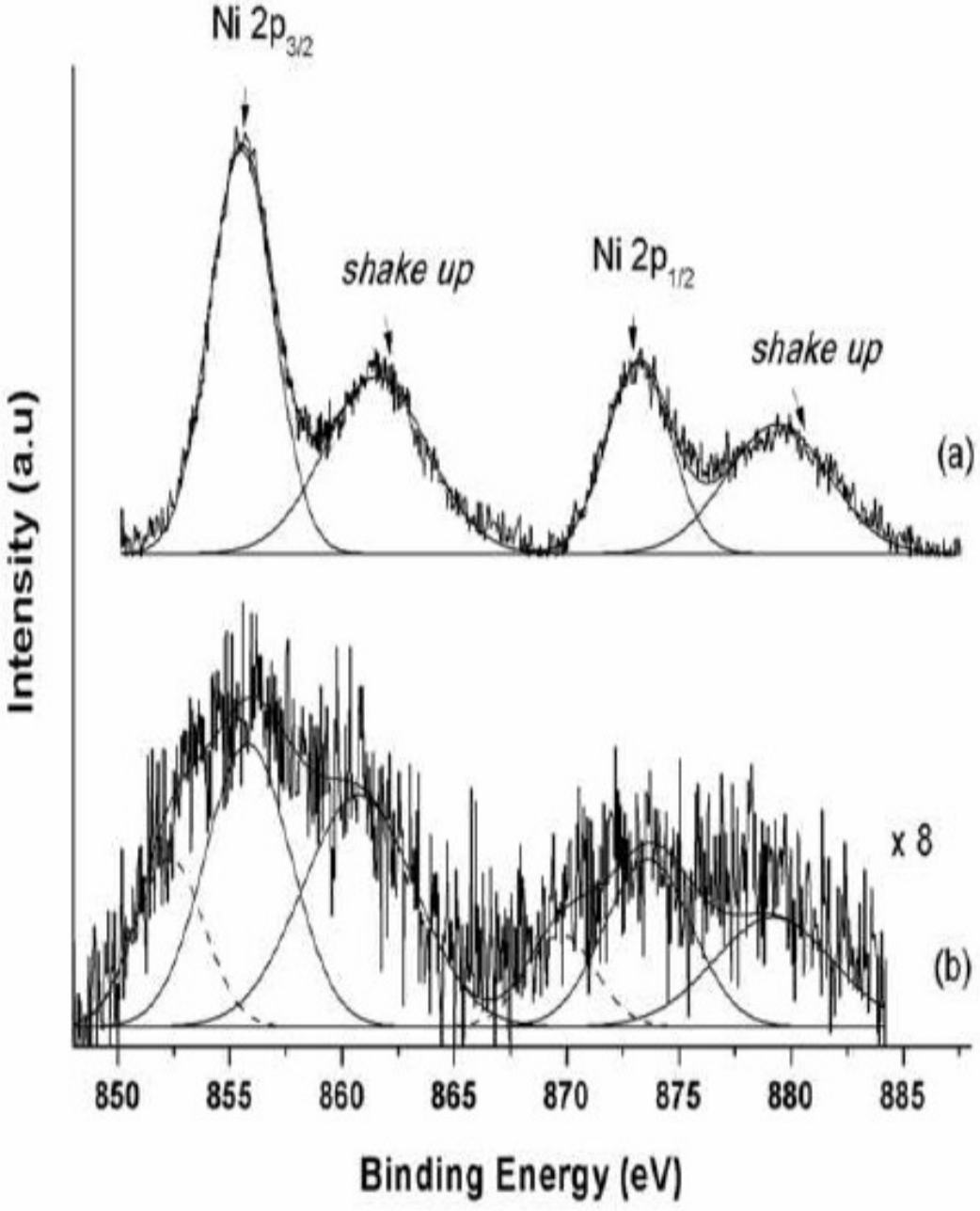

Figure 7. Au 4f and Mg 2s XP spectra of Ni-3Au catalyst as: (a) calcined and (b) after second TPR.

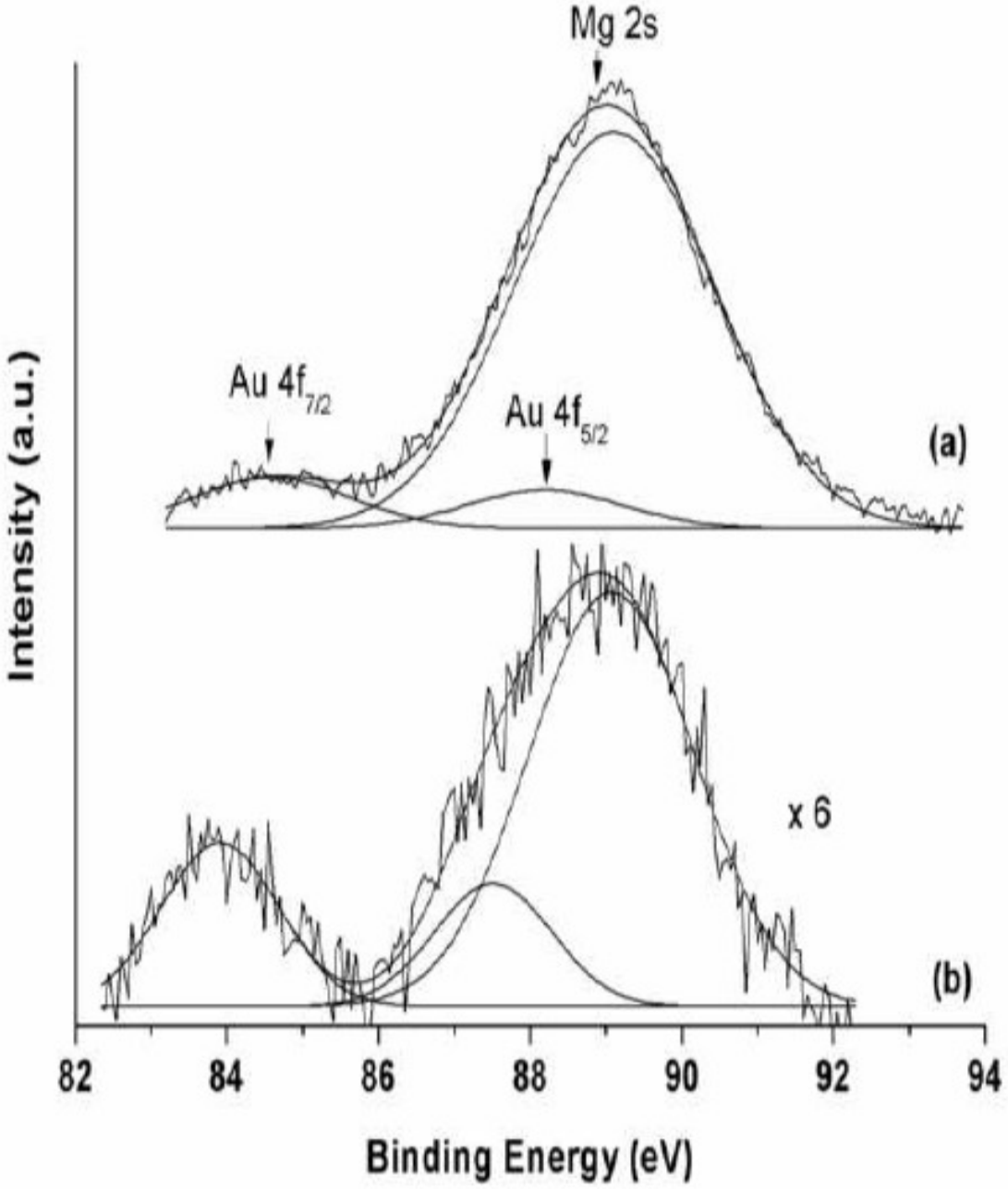

Figure 8. XRD patterns of Ni-3Au catalyst as: (a) calcined samples; (b) after first TPR; (c) after TPO; (d) after second TPR. The symbol * refers to the $MgAl_2O_4$ spinel peaks.

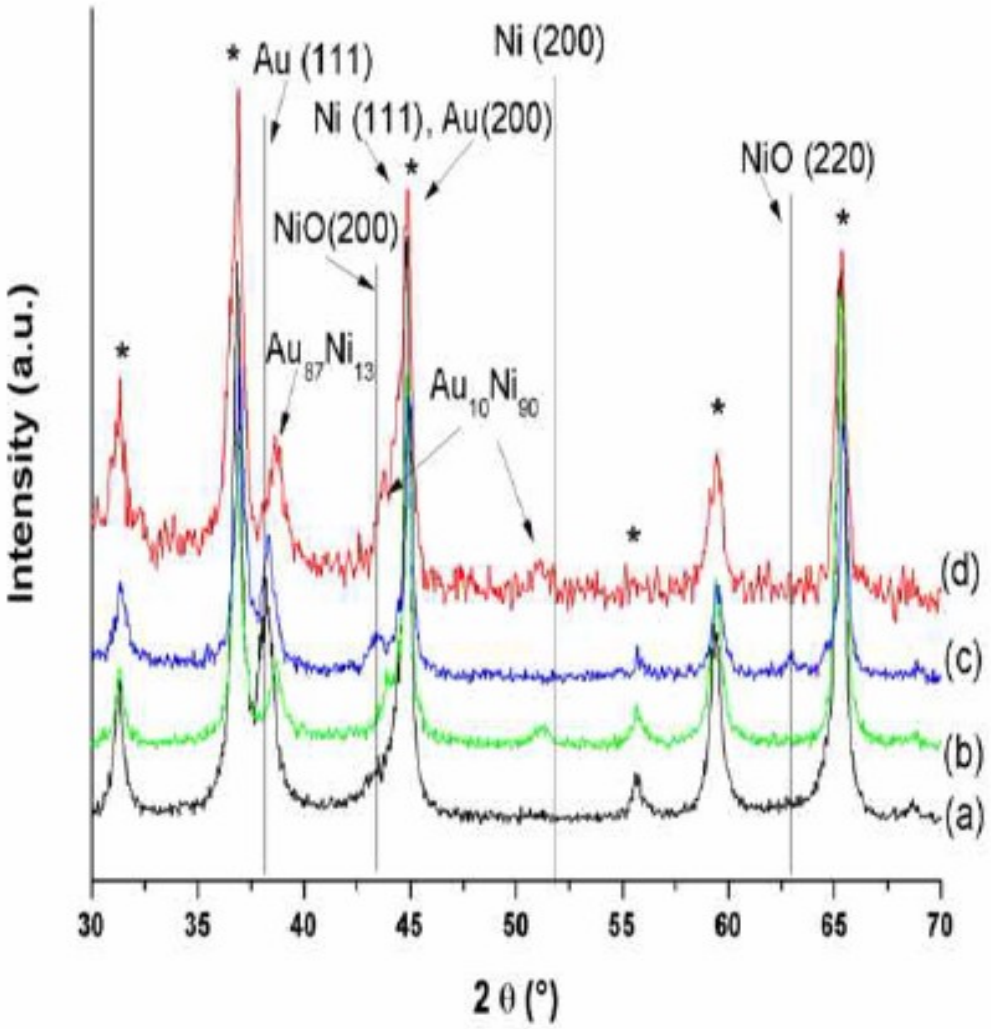

Figure 9. HRTEM image of Ni-3Au catalyst after TPR2.

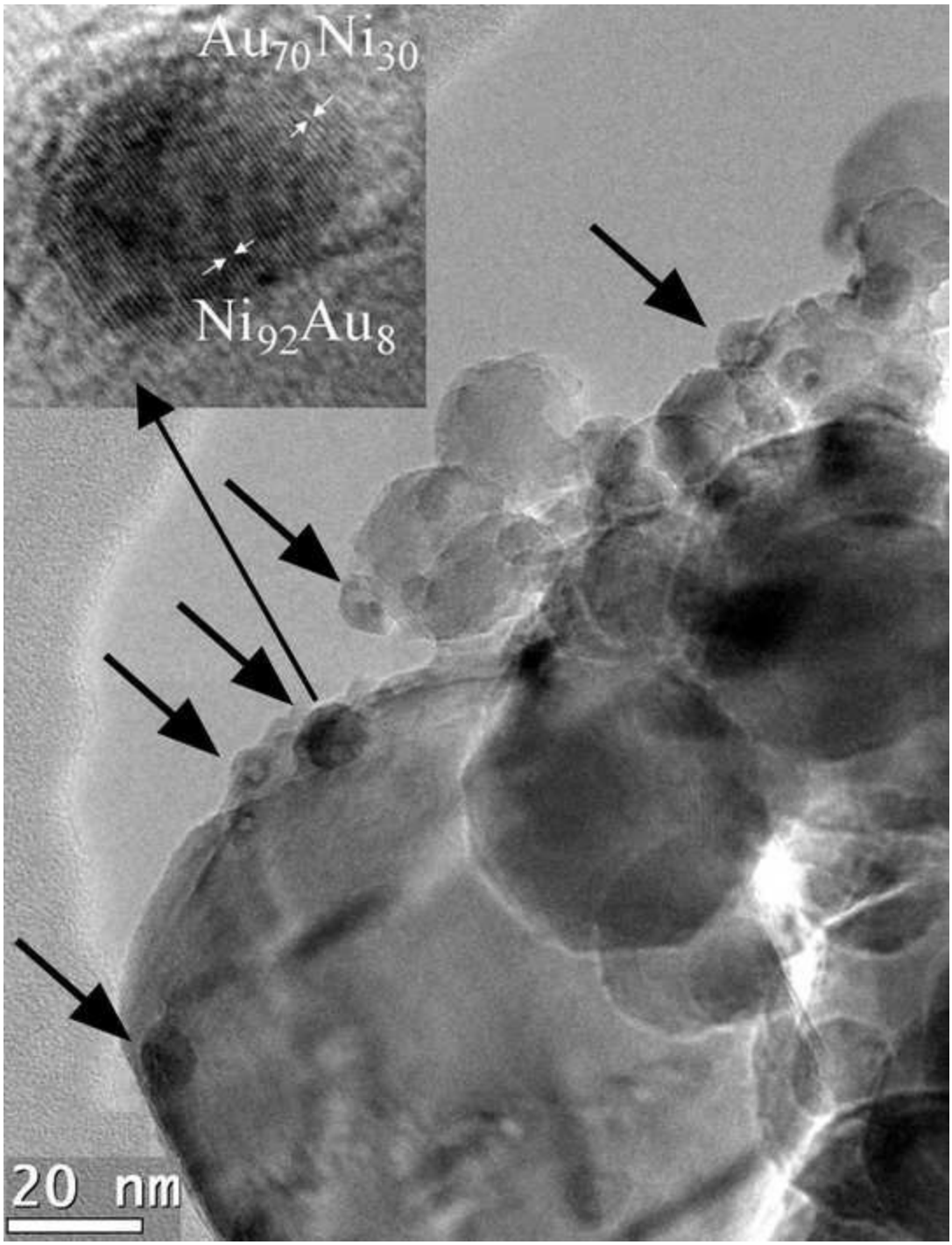

Figure 10. CH_4 (filled symbols) and CO_2 (empty symbols) conversion percentages as function of temperature over the different catalysts. F= 20 ml/min, W_{cat}=30 mg, feed gas composition: 69 vol% CH_4, 30vol% CO_2 and 1 vol% Ar.

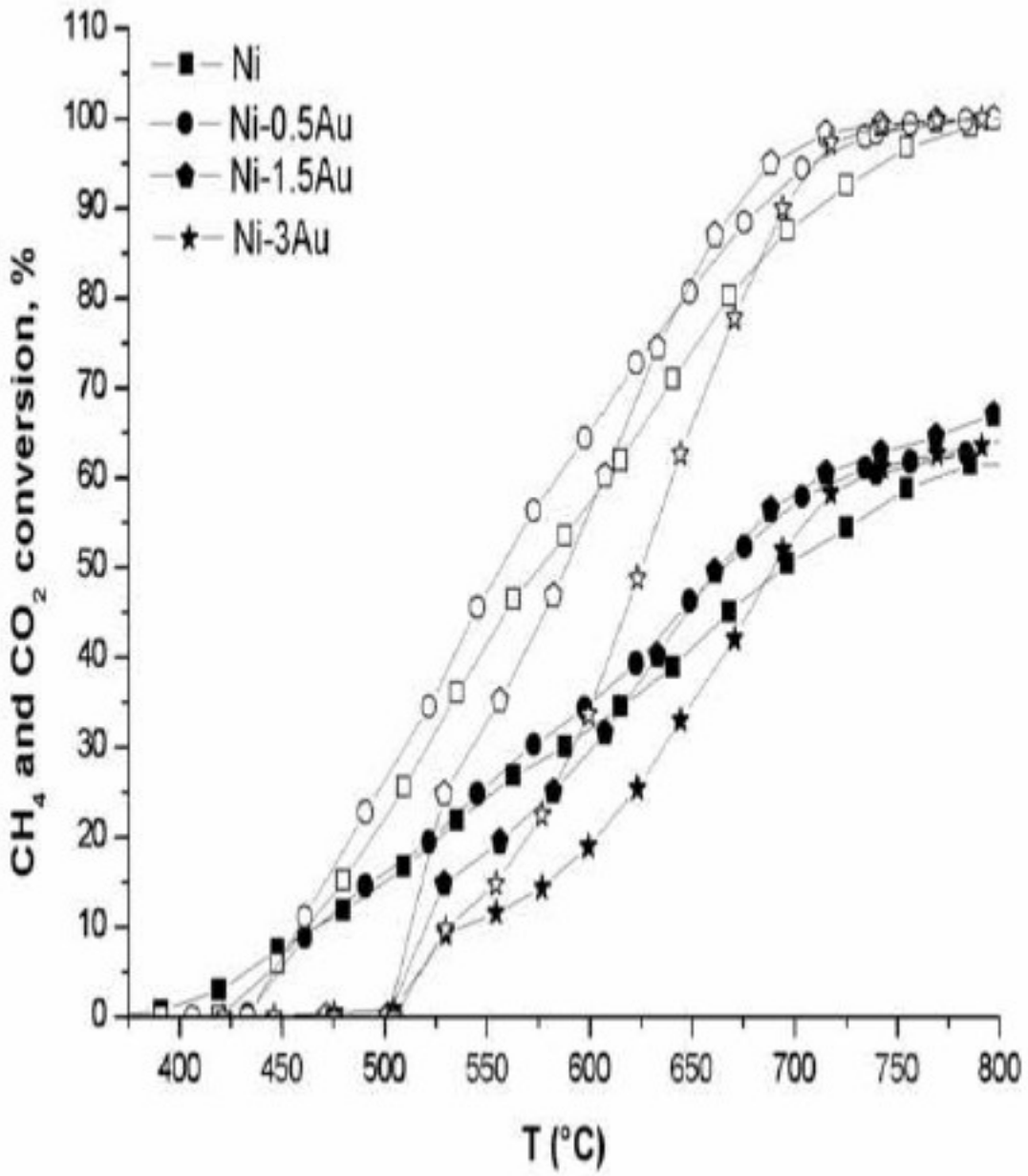

Figure 11. CH_4 (square) and CO_2 (circle) conversion percentages as function of temperature over Ni and Ni-3Au catalysts during the first run (filled smbols) and second run (open symbols). The corresponding CO/H_2 ratios are plotted in the lower part of the figure. F= 20 ml/min, W_{cat}=30 mg, feed gas composition: 69 vol% CH_4, 30vol% CO_2 and 1 vol% Ar.

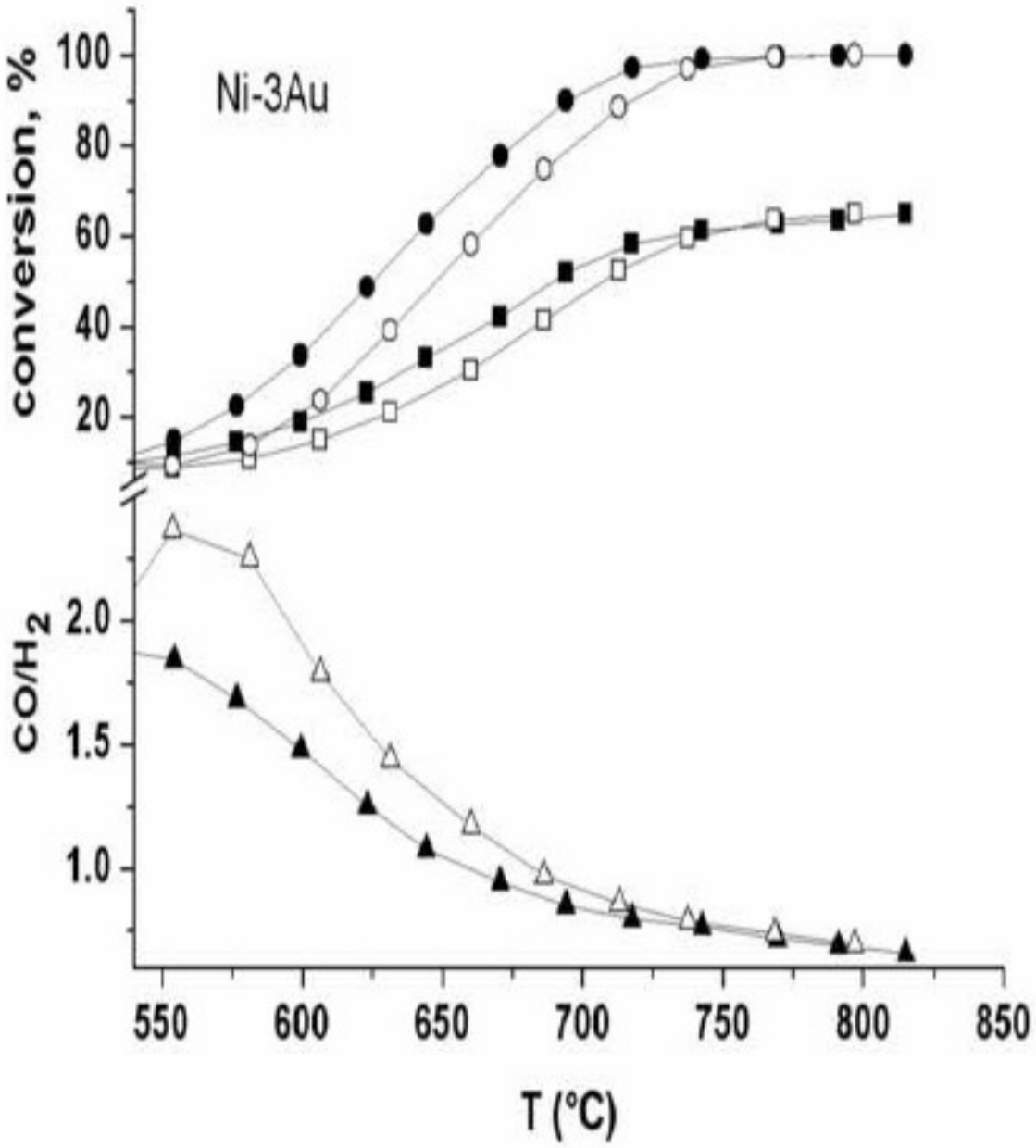

Figure 12. CH_4 (filled symbols) and CO_2 (empty symbols) conversion percentages during CO_2 reforming at 650 °C as a function of the time on stream measured over the monometallic and the bimetallic catalysts. F= 20 ml/min, W_{cat}=30 mg, feed gas composition: 69 vol% CH_4, 30 vol% CO_2 and 1 vol% Ar.

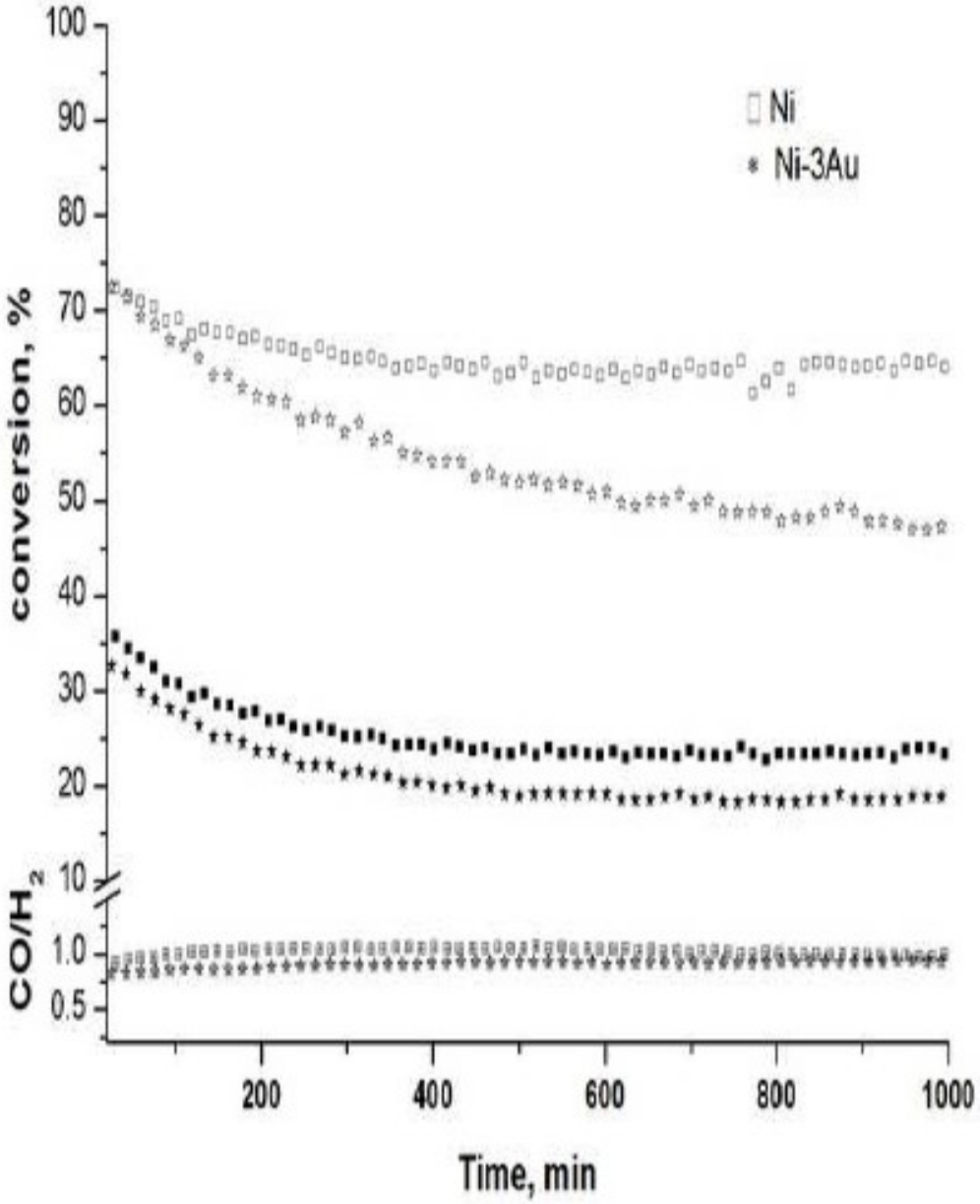

Figure 13. TEM image of the bimetallic Ni-0.5Au after the second DRM reaction. The Ni/Au ratio determined by EDS is indicated.

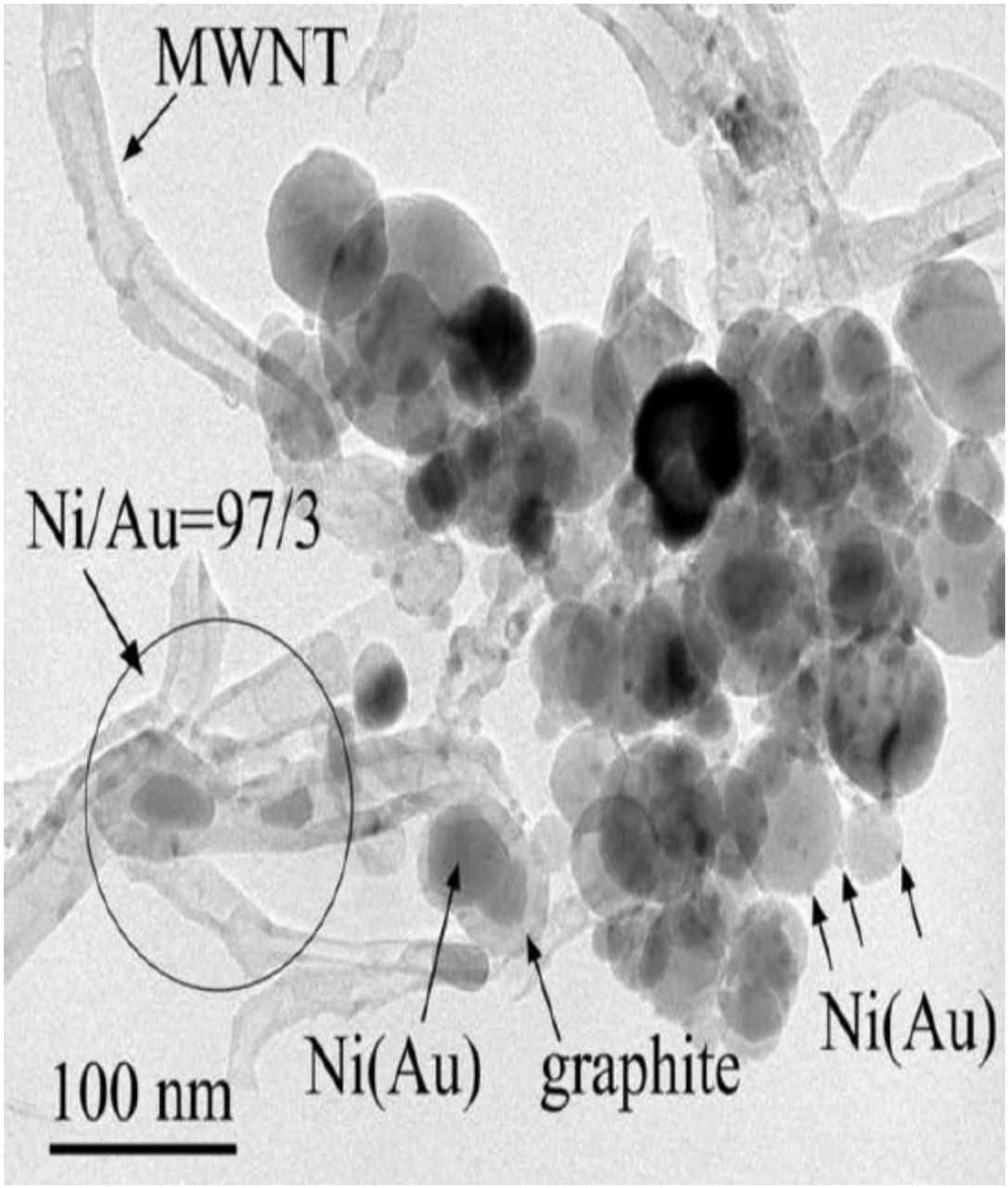

Figure 14. TPO curves of removed carbon from the catalyst surface after the first reaction.

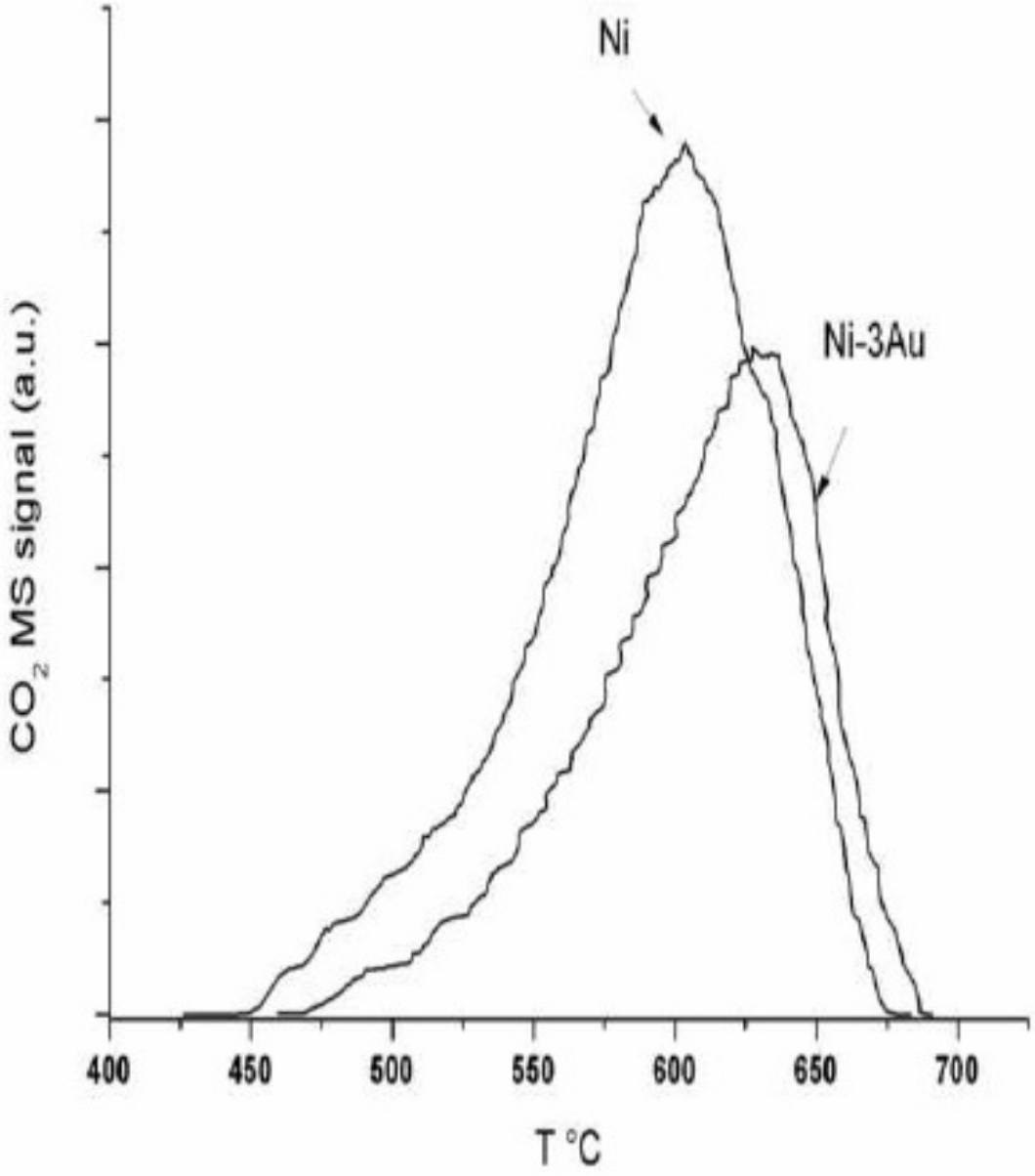

Tables

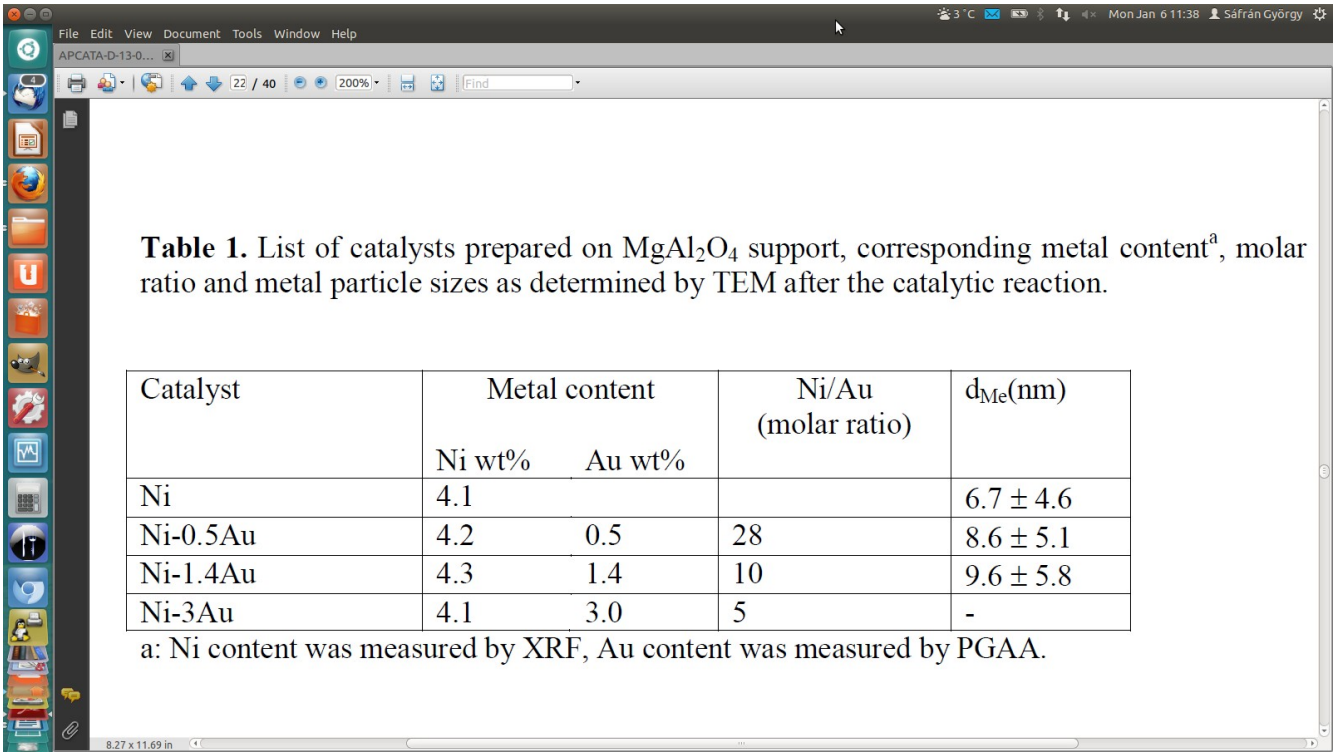

Table 1. List of catalysts prepared on $MgAl_2O_4$ support, corresponding metal content[a], molar ratio and metal particle sizes as determined by TEM after the catalytic reaction.

Catalyst	Metal content		Ni/Au (molar ratio)	d_{Me}(nm)
	Ni wt%	Au wt%		
Ni	4.1			6.7 ± 4.6
Ni-0.5Au	4.2	0.5	28	8.6 ± 5.1
Ni-1.4Au	4.3	1.4	10	9.6 ± 5.8
Ni-3Au	4.1	3.0	5	-

a: Ni content was measured by XRF, Au content was measured by PGAA.

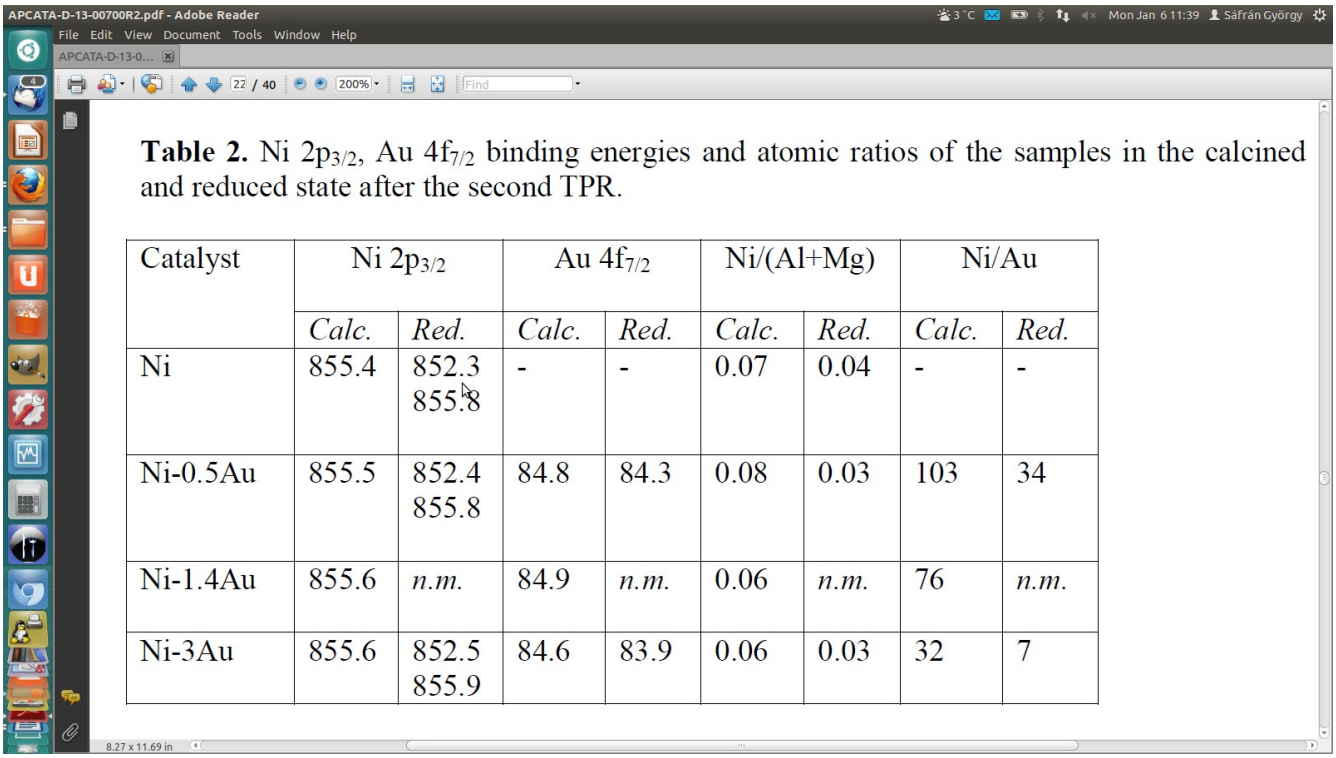

Table 2. Ni $2p_{3/2}$, Au $4f_{7/2}$ binding energies and atomic ratios of the samples in the calcined and reduced state after the second TPR.

Catalyst	Ni $2p_{3/2}$		Au $4f_{7/2}$		Ni/(Al+Mg)		Ni/Au	
	Calc.	*Red.*	*Calc.*	*Red.*	*Calc.*	*Red.*	*Calc.*	*Red.*
Ni	855.4	852.3 855.8	-	-	0.07	0.04	-	-
Ni-0.5Au	855.5	852.4 855.8	84.8	84.3	0.08	0.03	103	34
Ni-1.4Au	855.6	*n.m.*	84.9	*n.m.*	0.06	*n.m.*	76	*n.m.*
Ni-3Au	855.6	852.5 855.9	84.6	83.9	0.06	0.03	32	7